

**Nondestructive evaluation of aircraft skin lap splices for  
corrosion characterization using commercial eddy current instruments**

**by**

**Brian A. Lepine**

**A Thesis Submitted to the  
Graduate Faculty in Partial Fulfillment of the  
Requirements for the degree of  
MASTER OF SCIENCE**

**Department: Materials Science and Engineering  
Major: Metallurgy**

Signatures have been redacted for privacy

Signatures have been redacted for privacy

**Iowa State University  
Ames, Iowa**

**1994**

**TABLE OF CONTENTS**

<b>ACKNOWLEDGMENTS.....</b>	<b>v</b>
<b>CHAPTER 1. INTRODUCTION.....</b>	<b>1</b>
1.1. Problem Definition .....	1
1.2. Scope of Thesis .....	3
<b>CHAPTER 2. BACKGROUND.....</b>	<b>6</b>
2.1. Theoretical Developments .....	6
2.2. Previous Experimental Work.....	8
2.2.1. The development of corrosion measurements for lap splices .....	8
2.2.2. Calibration methods .....	11
<b>CHAPTER 3. EXPERIMENTAL SETUP AND MATERIALS.....</b>	<b>13</b>
3.1. Experimental Setup .....	13
3.2. Coils .....	15
3.3. Instrumentation.....	17
3.3.1. HP 4194A Impedance Analyzer.....	17
3.3.2. Commercial eddy current instruments .....	18
3.4. Materials and Corrosion .....	21
3.4.1. Aluminum alloy plate samples with machined flat bottom holes .....	21
3.4.2. Corrosion in aluminum alloys and prepared samples ..	23

<b>CHAPTER 4. THEORY .....</b>	<b>31</b>
4.1. Introduction to the Principles of Eddy Current Testing .....	31
4.2. Theory of Eddy Current Phenomenon.....	34
4.3. Skin Effect .....	37
4.4. Forward Solution for the Impedance of a Coil Over a Multi-Layered Half-Space.....	39
4.5. Swept Frequency Analysis of Corroded Lap Splices .....	43
4.6. Inversion Procedure.....	47
4.7. Commercial Eddy Current Instruments and Test Coil Signals .	48
<b>CHAPTER 5. CALIBRATION.....</b>	<b>59</b>
5.1. Introduction .....	59
5.2. Methods.....	60
5.2.1. Calibration procedure.....	60
5.2.2. Quantitative flaw measurements.....	63
5.3. Calibration Curves for Instrument A .....	63
5.4. Calibration Curves for Instrument B .....	65
5.5. Important Observations.....	65
<b>CHAPTER 6. QUANTITATIVE ANALYSIS OF THINNED ALUMINUM LAP SPLICES .....</b>	<b>70</b>
6.1. Introduction .....	70
6.2. Swept Frequency Impedance Measurements Of Machined Samples Using Air-core Eddy Current Probes .....	71
6.2.1. Impedance analyzer measurements and results .....	71
6.2.2. Instrument A measurements and results .....	79

6.2.3. Instrument B measurements and results .....	79
6.2.4. Inversion of experimental data.....	81
6.3. Corrosion Sample Measurements.....	88
6.3.1. Procedure.....	88
6.3.2. Inversion results.....	89
6.4. Experimental Measurements Using Ferrite-core Probes .....	92
6.4.1. Comparison of ferrite-core to an air-core coil .....	92
6.4.2. Discussion.....	93
<b>CHAPTER 7. CONCLUSIONS.....</b>	<b>96</b>
7.1. Summary.....	96
7.2. Future Work.....	99
<b>BIBLIOGRAPHY.....</b>	<b>101</b>
<b>APPENDIX A ACCELERATED CORROSION CHAMBER TESTS ..</b>	<b>104</b>
<b>APPENDIX B TABULATED EDDY CURRENT INVERSION RESULTS FOR THE MACHINED SAMPLES.....</b>	<b>105</b>
<b>APPENDIX C GRAPHED EDDY CURRENT INVERSION RESULTS.....</b>	<b>109</b>

## ACKNOWLEDGMENTS

I would like to extend my appreciation to John Moulder for his continuous support and sincere interest in my research. His technical advise has been invaluable and I can attribute the successful completion of my thesis to his guidance and willingness to help.

I would also like to thank my major professor, Dr. Bruce Thompson, who provided much needed enthusiasm and guidance during the course of my research, despite his busy schedule. Likewise, I want to thank Dr. David Hsu, Dr. Satish Udpa and Dr. Krishna Vedula for serving on my graduate committee.

The material in this thesis is based upon work performed at the FAA Center for Aviation Systems Reliability operated by Iowa State University and supported by the Federal Aviation Administration under Grant No. 93-G-018. Also, this graduate program was sponsored by the Canadian Armed Forces and their support is gratefully acknowledged.

Finally, I would like to thank my wife, Barbara, for her constant encouragement and support during the past two years.

## CHAPTER 1. INTRODUCTION

### 1.1. Problem Definition

Corrosion has long been one of the biggest maintenance and repair problems in the aircraft industry. As aircraft age, their maintenance costs increase and one of the major cost drivers is structural damage due to corrosion. Because of this widespread problem, preventive maintenance programs demand sophisticated and reliable inspection techniques capable of detecting corrosion in its earliest stage so that less expensive repair measures can be taken to arrest its progression. Modern nondestructive techniques have been widely used and studied in response to this demand, especially for corrosion in aircraft skins. Eddy current testing is often used to detect areas of a specimen that exceed a set threshold of metal loss due to corrosion. In most conventional techniques this is done by calibrating the test setup with a reference standard in a way that will correlate the output signal to a known and standard change in layer thickness. The eddy current signals can be displayed and interpreted to eliminate signals arising from unwanted sources, such as lift-off, and to detect certain flaws that exceed a predetermined amount, such as 10% corrosion thinning.

Typically, corrosion is relatively easy to detect in single layered structures when given such a criteria. However, multi-layered structures, such as lap splices that consist of two thin skin aluminum alloy layers riveted together are more difficult because of the increased number of possible locations and ways that the corrosion can occur between and beneath the

layers. A pass/fail detection criterion can still be established with multiple frequency measurements, but, these standard methods are not well suited to completely characterize a structure in a quantitative manner. For example, it is extremely difficult for conventional techniques to determine the amount and location of metal loss due to corrosion in aircraft lap splices and actually infer the thickness of each layer in the skin structure, including the air gap. Nor can they easily distinguish corrosion-related air gaps from air gaps unrelated to corrosion, such as layer separation due to distortion, disbond, or a scrim cloth. Only quantitative nondestructive evaluation (NDE) techniques can perform these types of analyses, which makes their development more desirable to a maintainer who faces high-cost, corrosion-related maintenance and repair decisions.

In general, quantitative NDE requires quantitative measurements and a theory to interpret them. Theoretical eddy current NDE usually models the test coil's impedance change (in ohms) as the quantitative measure that varies with specimen and flaw parameters. Specific laboratory instruments such as impedance analyzers are capable of making quantitative measurements that allow researchers to compare experimental data directly to theory. But, typical in-field eddy current instruments are not capable of measuring probe impedances quantitatively. Rather, they measure relative changes in the coil impedance. Thus, there is a strong need for ways to apply the techniques that are developed in the lab to the instruments that are currently available in the field.

## 1.2 Scope of Thesis

This thesis will examine and evaluate recently developed eddy current corrosion characterization techniques for the very common lap splice configuration found in many aircraft skin structures. Additionally, finding a link between the development and the actual implementation of these methods in the field is an important goal. This can be done by adapting the methods to existing commercial eddy current instruments. Instrumentation concepts are studied, leading to a generic calibration procedure that will allow them to make quantitative impedance measurements, such as those required to characterize corrosion in lap splices as well as other types of flaws. Their accuracy and effectiveness will be evaluated for swept frequency measurements.

Chapter 2 gives an initial survey of the present state of this technology in terms of the theoretical and experimental work performed previously by many scientists and researchers. The remainder of this thesis builds on many of these accomplishments. Chapter 3 presents the experimental setup and equipment that were necessary in developing the calibration procedures and evaluating the corrosion measurement techniques. An explanation of the corrosion mechanisms in aluminum-copper alloys is included in this chapter.

Chapter 4 focuses on the theoretical models used in the course of this research. The basic principles of eddy current testing are discussed and Maxwell's equations are presented. The forward solution developed by Uzal and Moulder [1] that models the coil's impedance change when placed over a lap splice with and without corrosion is reproduced. This is based on the important eddy current coil theories first presented by Dodd and Deeds [2],

then by Cheng, Dodd and Deeds [3]. Some theoretical curves for the coil's resistance change with frequency are presented to illustrate the distinctive features that depend on the location and the amount of thinning in lap splices. Also, simple bridge circuit analysis shows that a test coil signal is a voltage magnitude that is proportional to an impedance change. This relationship can be found by calibrating the instrument with a series of resistors switched into the coil's circuit. Hence, any signals due to any flaws can be expressed quantitatively as impedance changes. Chapter 5 applies this knowledge experimentally and presents a simple method for calibrating almost any commercial eddy current instrument. Results are given for two separate instruments, A and B, along with some important observations that characterize the behaviour of these particular units.

Chapter 6 compares experimental lap splice corrosion swept frequency measurements made with an impedance analyzer to the theory's forward solution. Effects such as coil size and layer separation are also analyzed. Mainly air-core probes are used to allow comparisons of experimental data to theory. However, ferrite probes are also included for completeness; a brief look at the ferrite's effect is taken from a purely empirical perspective. The technique is then applied using the calibrated commercial eddy current instruments, where the results are compared to both theory and the impedance analyzer. Given that the theory and experimental data agree well for a known air-cored coil, the data can be inverted to infer the amount of thinning by inferring the thickness of each layer in the skin structure. A method is borrowed from Moulder and Uzal [4] who used a simplex direct search procedure that solves for the forward solution while changing the specimen's

parameters repeatedly until a match with the test data is found. Inversion results are given for samples with machined air gaps and for corrosion samples produced artificially from accelerated electrochemical methods. The actual thicknesses are compared to those inferred by measurements from the impedance analyzer and instrument A.

Chapter 7 summarizes the findings and presents some concluding remarks. Possible future work is identified such as more in-depth study of ferrite-core coils and the need to refine these methods so that fewer frequency points need to be measured, thus enhancing the practicality of use of commercial eddy current instruments.

## CHAPTER 2. BACKGROUND

The experimental work done in the past will be briefly described while referring to the researchers' findings regarding their comparisons to theoretical predictions. The swept frequency techniques utilized in this thesis were essentially experimental developments that could be modeled analytically. The relevant theoretical work was a minor development of existing theory and a description of their evolution will precede that of the experimental work.

### 2.1. Theoretical Developments

Much work has been done on modeling eddy current phenomena in various applications that allows quantitative measurements to be interpreted and used for quantitative analysis. Ideally, this would always be accomplished through closed form analytical solutions that can represent probe signals in terms of the test specimen parameters. However, only the simplest NDE problems can be solved analytically. Awkward boundary conditions associated with irregularly shaped defects and interfaces in practical eddy current testing situations preclude the use of analytical models. In such circumstances, numerical modeling approaches, such as the boundary element, volume element or finite element methods, are used instead; examples of their application in eddy current NDE can be found in [5,6], [7] and [8] respectively.

The detection and characterization of corrosion in lap splices with eddy currents, however, is one exception that can take advantage of exact solutions because of the relatively simple axisymmetric geometry. The relevant

theoretical work for this case is actually a minor development of existing theory for a coil located over a layered infinite medium. Initially, Dodd and Deeds [2] developed a theoretical model for the impedance of a coil over a two-layered, half-space conductor. Then Cheng, Dodd and Deeds [3] generalized this method for multi-layer problems, using a transfer matrix method to handle the large number of equations that arise from the need to solve for the solution's coefficients using boundary conditions at each interface.

Moulder *et al.* [9] developed an analytical model, based directly on Dodd and Deeds' theory, that could determine the thickness and conductivity of a uniform conductive layer on a substrate metal. This was based on the coil's impedance difference between the presence and absence of the layer. It was found that the real part of the coil's impedance change,  $\Delta R$ , had considerable structure when plotted vs. frequency. The typical response started from zero at zero frequency and decreased to form a minimum, then increased monotonically after crossing the zero axis. The frequency of the minimum and the zero in  $\Delta R$  depended strongly on the top layer thickness and the electromagnetic properties of both the layer and the substrate. These authors hypothesized that the layer thickness and conductivity could be determined by an inversion method that was based on the frequency dependence of the experimentally measured impedance difference and the forward solution's formula for that change.

Uzal *et al.* extended this conductivity-thickness method to the more complex case of a multi-layered material whose conductivity and permeability vary arbitrarily through the thickness of the material [10]. For this solution,

they used an exact numerical method that required the transfer matrix approach of [3]. They later adapted this technique to model a coil over a four-layer configuration that represented the metal and air gap layers of an aircraft skin lap splice thinned due to corrosion [1]. It is on this model that the majority of this thesis is based.

## **2.2. Previous Experimental Work**

### **2.2.1. The development of corrosion measurements for lap splices**

In the conductive layer thickness study of Moulder *et al.* [9], experimental swept frequency measurements of the difference in a coil's impedance associated with the presence and absence of the layer were made for a variety of thicknesses. The frequency dependence of the resistive (real) component of the impedance agreed well with theory. In addition, an inversion procedure was developed that focused on the coil's resistive changes in the frequency domain since it was found that the frequency of the minimum and the zero in  $\Delta R$  depended strongly on layer thickness and the electromagnetic properties of both the layer and the substrate. This procedure consisted of a numerical inversion method that would find the layer's parameters for which the theory curve best matched the experimental data. Generally, the thicknesses and conductivities were inferred with good accuracy. The results of [9] emphasize the need for accurate quantitative measurements when using eddy current data to determine material properties. It is important to realize that the success of this or any other quantitative eddy current technique relies heavily on the ability to make quantitative

measurements, such as with an impedance analyzer, as well as the use of precisely wound air-core coils that can be modeled accurately.

Mitra *et al.* [11] performed similar quantitative swept frequency measurements on various configurations of two aluminum alloy plates with machined shallow flat-bottomed holes to simulate loss of metal from corrosion. These regions were oriented in four different ways to simulate an aircraft skin lap splice with hidden corrosion in four different locations. The flat-bottomed holes were placed on the bottom of the first (top) layer, the top of the second layer, on the faying surface of both layers at once, and the bottom surface. This work compared experimental curves with the theory analysis of Uzal *et al.* [1] for these special cases, and showed good agreement. Additionally, specific features in the swept frequency response curves were examined in relation to the various amounts of metal loss, or thinning, and its locations. Figure 2.1 illustrates a typical theoretical swept frequency response curve; in this case, the coil's resistance change,  $\Delta R$ , is the result of placing it over a specimen in the absence and presence of second layer thinning. All curves generally exhibited a minimum in the resistance change,  $\Delta R_{\min}$ , as well as two zero crossings. It was found that the frequency of the minimum in particular could be used to determine the layer in which the corrosion occurred. The minimum shifts towards a lower frequency as the location of the thinning moves from the first to the second layer, then to the bottom surface. The magnitude of the minimum was then used to create calibration curves of  $\Delta R_{\min}$  vs. depth of machined region, that could infer the thinning for a given location. Results were obtained for the machined samples as well as electrochemically corroded samples, and the amounts of inferred metal loss for

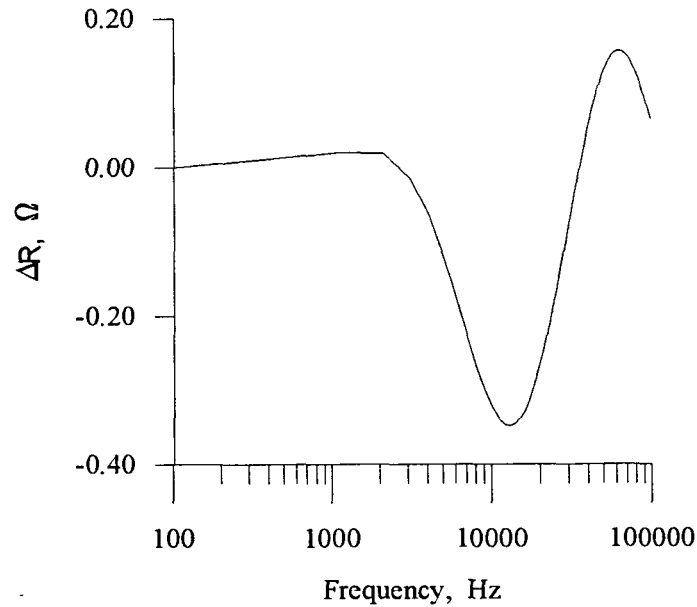


Figure 2.1: A typical theoretical swept frequency response curve for second layer thinning

two different locations were in good agreement with direct measurements.

Moulder and Uzal applied the numerical inversion method of [9] to the simulated lap splice corrosion problem. The eddy current measurements were performed in the same manner as by Mitra *et al.* The inversion routine was developed to determine the results in terms of the three layer sizes, namely: the thickness of the top layer, the air gap due to thinning, and, the second layer. The results for corrosion located in the first or the second layers were very good when compared to the actual dimensions. They also used this method on an actual Boeing aircraft skin sample, but found that some corrosion sites were too small to measure accurately since the coil's diameter was larger than the area of the corrosion.

### 2.2.2. Calibration methods

The eddy current NDT community depends on reference standards to calibrate or standardize a test setup before performing an inspection to obtain results that are consistent from day to day and between inspecting organizations [12]. Also, tests that must detect flaws over a certain size, or characteristic changes in a material, do so by correlating the output signal magnitude to a known reference standard. These kinds of calibration procedures do not lend themselves well to the application of quantitative NDE. For the purpose of this thesis, calibration relates the response of an instrument to a fundamental unit of measurement which, in this case, is the unit of electrical impedance in ohms.

Moulder *et al.* looked at several calibration methods for eddy current measurement systems. In [13], one of the methods electrically calibrated a system by inserting small resistances in series with the eddy current probe. The system consisted of a broad-band inductive bridge connected to two similar air-core coils in a differential configuration, with a signal source to drive the circuit. A calibration box containing several resistors from 0.01 to 5 ohms, accurately measured with an impedance analyzer, was connected to the circuit so that the resistors could be switched into series with one of the coils. The magnitude and phase output signals were measured independently for two frequencies, 500 kHz and 1 MHz, at each resistor switch setting. The magnitude and phase of the bridge output voltage change,  $\Delta V$ , were plotted against the magnitude and phase of the calibrating impedance; these plots were shown to be linear relationships at both frequencies. This illustrated that the response of the bridge is linear at a single frequency and that the whole eddy

current system could be calibrated in both magnitude and phase (or real and imaginary components) with small real impedance changes alone.

Eddy current instruments basically work with the bridge circuit principle, since the probes are connected in a differential configuration; therefore, these systems can also be calibrated in a similar fashion. As will be seen, when fully calibrated any eddy current instrument is capable of quantitatively measuring a coil's impedance change in any test configuration. Hence, the quantitative method for characterizing corrosion in lap splices developed with the use of an impedance analyzer can be adapted to these instruments. The obvious advantages of using these instruments, such as size, portability, cost, availability and familiarity for trained personnel, makes these developments attractive to the NDE community.

## CHAPTER 3. EXPERIMENTAL SETUP AND MATERIALS

### 3.1. Experimental Setup

The goals of this research require a great deal of measurement and analysis of experimental data. The overall process consisted of three separate experimental phases. The initial part of the experiments focused on determining the impedance of a coil placed over two 40 mil (1 mm) 2024-T3 alloy plates with and without simulated corrosion, using three different coils. The setup that accomplished this is illustrated in Figure 3.1. This first phase utilized the impedance analyzer which measures the total electrical impedance of the coil over the metal and its associated cable. The change in impedance  $\Delta Z$  of the probe caused by moving from an uncorroded area,  $Z'$ , to a corroded area,  $Z$ , was recorded by a PC computer for later analysis. Since the analysis requires that this impedance change be caused only by the changes in the test material, the two separate measurements must be otherwise consistent. The measurements were found to be sensitive to small amounts of lift-off and tilt; hence, a spring loaded jig was used that could place the probe back and forth onto a sample consistently with the same amount of pressure and lift-off while reducing tilt to achieve reproducible results.

The second phase concerned calibration of two commercial eddy current instruments in a way that would allow the output voltage signals to be converted to impedance changes in ohms. This was accomplished with the addition of a calibration box, shown as a dashed outline in Figure 3.1. The box, illustrated in more detail in Figure 3.2, is made up of eight resistors

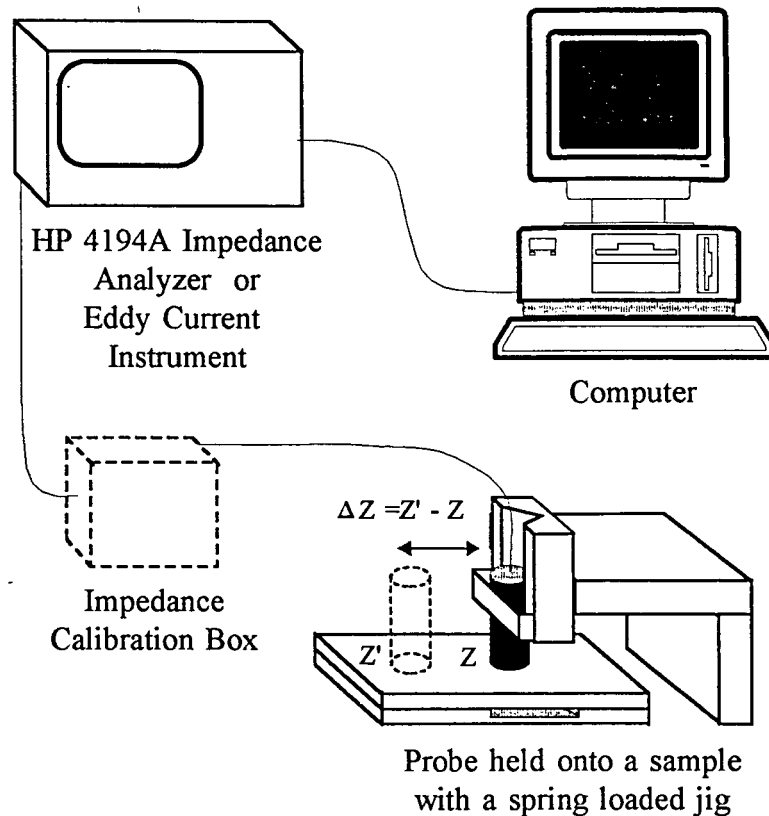


Figure 3.1: Setup for all experiments. The impedance calibration box is only used when calibrating the commercial eddy current instruments

ranging from  $0.01 \Omega$  to  $1.0 \Omega$  (nominally ohms), each connected in series with a switch. After accurately measuring the resistors with an impedance analyzer, only those with negligible inductance were used, narrowing the range from  $0.08$  to  $1.0 \Omega$ . During calibration, the resistors were switched into the circuit in series with the test coil and the eddy current instrument.

Phase three consisted of using two different eddy current instruments to measure the lap splices as in phase one. Thus, Figure 3.1 again shows the setup, replacing the impedance analyzer with either instrument A or B.

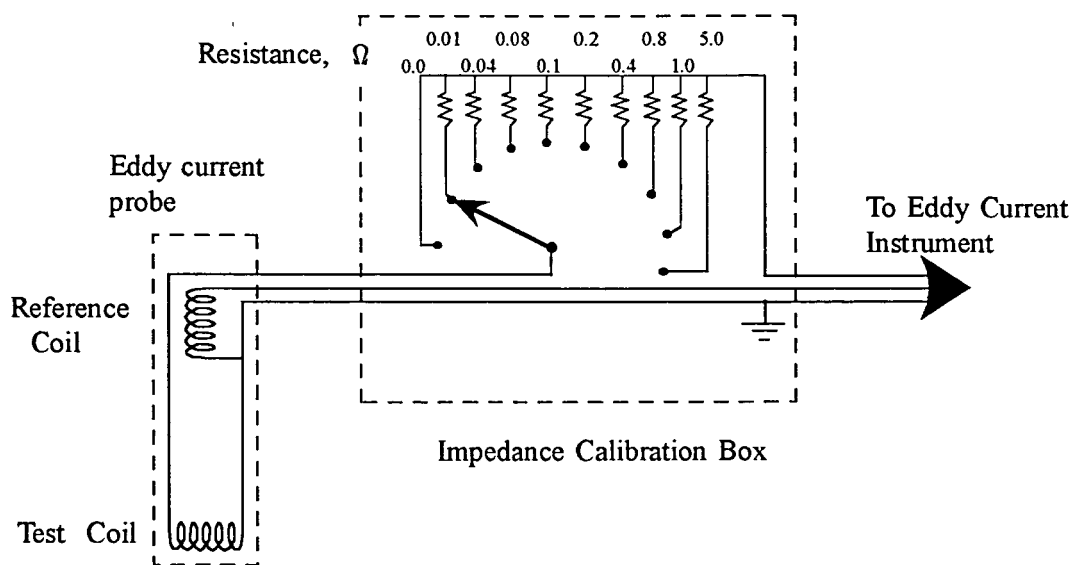


Figure 3.2: Impedance calibration box

### 3.2. Coils

The eddy current probe basically consists of a primary excitation wire coil with either an air or ferrite core. There are many different types of coils for various applications. For example, flat probe coils are used to test flat surfaces for conductivity, thickness and defects such as cracks or inclusions. Others such as encircling coils and inner coils are often used to test rods from the outer diameter, and tubes from the inner, respectively. Because the objective of this thesis is mainly to compare theory to experiments, precision wound coils were specially constructed by a commercial source that followed the design criteria and dimensions given in Table 3.1. The various parameters are illustrated in Figure 3.3. Two different diameter coils, ISU 2 and ISU 3, were each designed by setting their dimensions constant and calculating the number of turns required to obtain an inductance of  $530.5 \mu\text{H}$ . This ensured

Table 3.1. Parameters of the three precision wound coils

Coil parameters	Coil ISU 2	Coil ISU 3	Coil ISU 5
Inner radius (mm)	2.0	5.0	2.0
Outer Radius (mm)	4.0	7.0	4.0
length (mm)	2.0	2.0	2.0
Lift-off (mm)	0.25	0.45	0.25
Number of turns	319	186	319
Inductance ( $\mu\text{H}$ )	530.5	530.5	1225.0
Core	air	air	ferrite

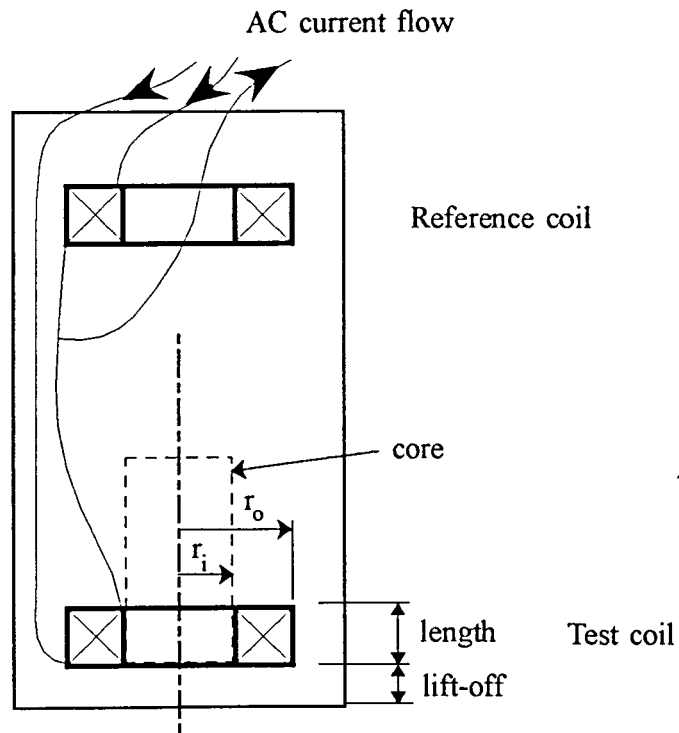


Figure 3.3: Probe with reference and test coil cross sections

that they matched the eddy current instrument's input impedance of 50 ohms at 15 kHz; this is the center frequency of the range in which lie the strongest signals,  $\Delta R_{\min}$ , due to corroded 40 mil 2024 lap splices. These special probes were also constructed to accommodate commercial eddy current instruments by providing each test coil with a matching reference coil located away from the test coil, both within the probe's casing. This allows the probes to be connected in a differential configuration.\* Note that the reference coil is usually oriented at  $90^\circ$  to the test coil to avoid any coupling between them. The lift-off is a measure of the built-in distance between the bottom of the coil and the bottom portion of the probe casing as shown in Figure 3.3.

Two ferrite-core probes were also constructed with the same parameters as their respective air-core coils. However, only one ferrite-core probe, ISU 5 given in Table 3.1, was used in this research.

### 3.3. Instrumentation

#### 3.3.1. HP 4194A impedance analyzer

The model 4194A impedance analyzer manufactured by Hewlett Packard is an instrument capable of measuring complex impedances at frequencies from

---

\* This must not be confused with differential probes. Most texts and manufacturers refer to differential probes as having two identical coils placed over a specimen (or encircling a rod, or inside a tube) so that a null signal is obtained if they are each subjected to identical test specimen conditions. Absolute probes only have one coil placed over the specimen at one time, as in our case.

100 Hz to 100 MHz. In all of the measurements, this instrument was set to take 64 averages with medium integration time to reduce electronic noise. The integration time sets the sample rate. The instrument's precision is 10 milliohms ( $m\Omega$ ) for the impedances and conditions used in the measurements reported in this thesis.

### 3.3.2. Commercial eddy current instruments

Two instruments from different commercial sources, A and B, were calibrated in phase two and used for the corrosion measurements of phase three. Figure 3.4 gives a simplified block diagram of instrument A showing the circuit configuration when a normal probe is connected to the pins labeled A to D. Although instrument circuits vary greatly depending upon their application, most, including instruments A and B, generally use the AC bridge circuit concept illustrated in Figure 3.5 [14]. Here, the test coil is used as one of the arms in the bridge circuit. The connector pins of Figure 3.4 are also indicated here for cross-reference. In the common differential configuration, the reference coil's impedance is represented by  $Z_1$ . These models obviously lack the details that make up an actual instrument's circuits and systems since they are only meant to illustrate typical eddy current instrument concepts.

Unlike an impedance analyzer, most eddy current instruments only measure relative signal changes. Before performing a test, the instrument is nulled with the probe on a normal reference material, such as on an area of a lap splice without corrosion. The nulling operation balances the bridge circuit with a compensating signal, not shown in the preceding diagrams, that brings

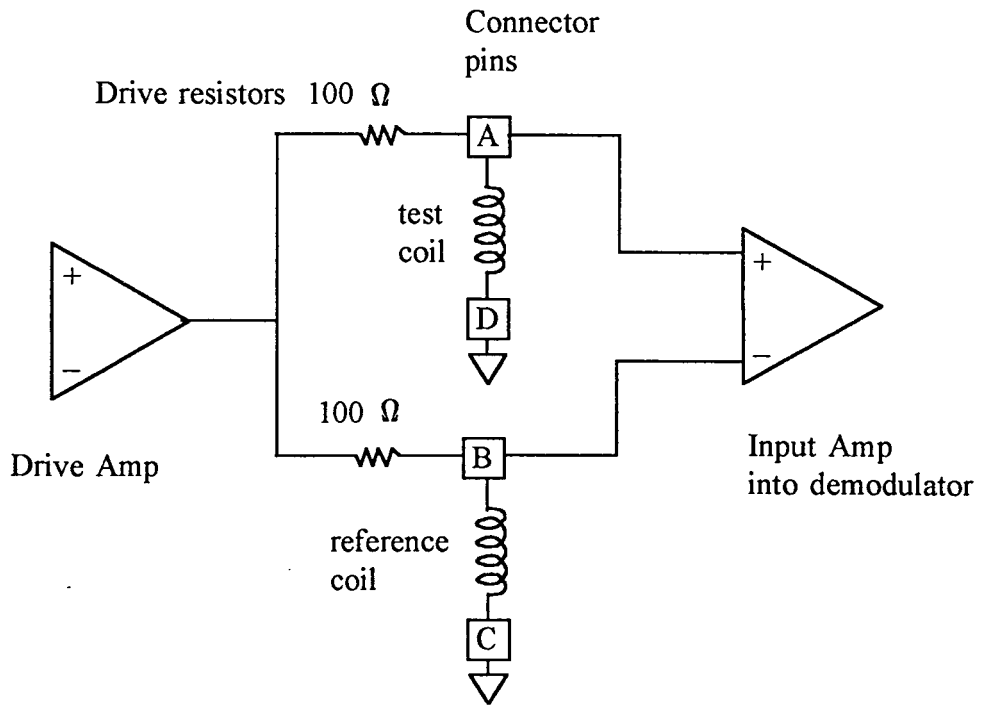


Figure 3.4: Block diagram for Instrument A with a probe connected in a differential configuration

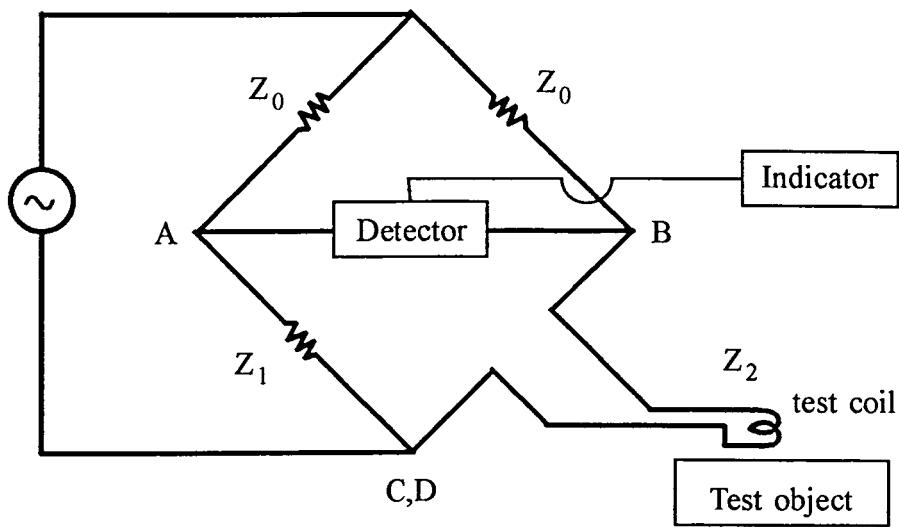


Figure 3.5: Test coil bridge circuit [14]

the operating point to a reference position; hence, the output signal due to a flaw or other factor, such as lift-off, is a deviation from this reference. This imbalance shows up on the indicator, usually a CRT display screen on most modern eddy scopes, as impedance plane trajectories representing changes in the coil's impedance in both magnitude and phase. The output signals, therefore, consist of both voltage magnitudes and phase angles [14]. Conventional tests often involve rotating the phase angle manually until an unwanted signal, such as lift-off, is horizontal; any pertinent signals with a vertical component, therefore, can usually be detected and identified.

Usually only one frequency can be measured at once, such as with instrument B; however, instrument A can measure four frequencies simultaneously. For this reason, most of the results in chapter 6 for the lap splice measurements are from instrument A. Each instrument is equipped with variable output signal gain settings that can be selected to amplify weak signals, such as those due to a small flaw. They were checked and found to be linear and accurate before performing the calibration and corrosion inspection tests.

Also, a probe drive option gives control over the amount of AC source voltage that drives the eddy current probe. This was kept constant for instrument A at 8 volts peak-to-peak, and "mid" drive for instrument B, for all experiments.

### **3.4. Materials and Corrosion**

#### **3.4.1. Aluminum alloy plate samples with machined flat-bottom holes**

The specimens inspected by the eddy current tests consisted of two 3x5 inch, 40 mil thick 2024-T3 aluminum alloy plates forming two layers representative of those typically used in aircraft skin lap splices. These samples are classed into two categories: machined and corroded. Throughout the majority of the eddy current quantitative measurements in this thesis, the machined flat-bottom hole shown in Figure 3.6(a) shall represent the thinned regions in the lap splices because the theory models the corrosion in this way. Note that the diameters of the coils were all less than the smallest lateral dimension of the flat-bottom holes. A variety of 40 mil thick plates were used with hole depths nominally ranging from 2 mils to 16 mils to simulate various amounts of thinning due to corrosion. The actual depths are given in Table 3.2. Some of the holes' depths vary slightly from one end of the slot to the other. Thus, the tabulated data have been averaged from three different micrometer readings. On occasion, thinning may be referred to in terms of a percentage of the structural plate thickness. For example, the aircraft industry usually demands that an NDT method detect a minimum of 10% thinning of the outer skin. For a lap splice made up of two 40 mil plates, 10% thinning in any region is equivalent to 4 mils of metal loss.

We made measurements for simulated corrosion in four different locations in the two layered lap splices. Figure 3.7 shows these four configurations, namely: first (top) layer, second layer, both layers symmetrically thinned, and bottom surface. Note that the matching pairs of 2,

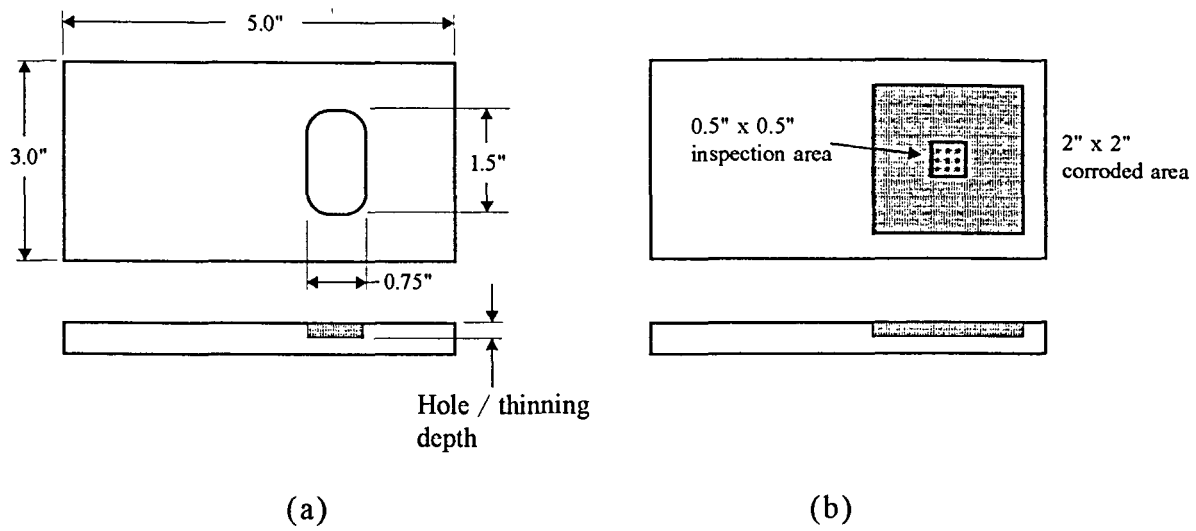


Figure 3.6: 40 mil 2024-T3 plates with thinned regions represented by (a) a machined hole and (b) artificially corroded areas

Table 3.2. Actual machined hole depths of samples in Figure 3.6(a)

Plate number	Nominal depth (mils)	Actual average depth (mils)
2A	2	2.8
2B	2	2.5
4A	4	4.5
4B	4	4.5
8A	8	8.0
8B	8	8.5
10B	10	10.0
12B	12	12.0
16B	16	16.0

4 and 8 mil plates (A and B) in Table 3.2 are used to simulate the symmetrical thinning of Figure 3.7(c); otherwise, a normal plate is combined with a machined one to produce the other simulations. During testing, the single plates are held in place in pairs by an acrylic fixture that mounts them away from any interfering metal and holds them flat.

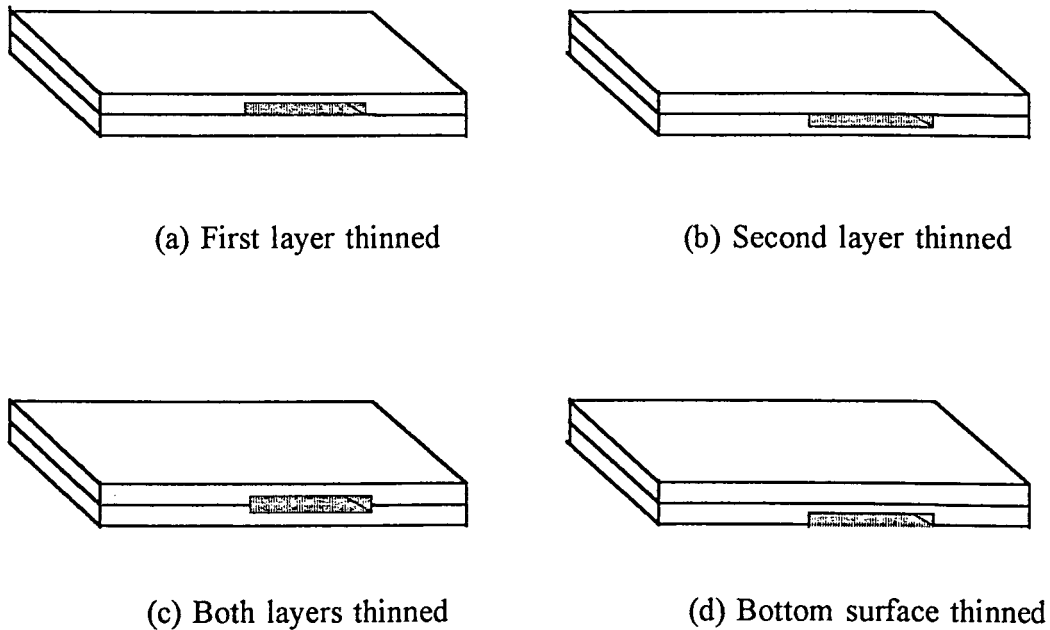


Figure 3.7: Four locations of thinning due to corrosion in lap splices

### 3.4.2. Corrosion in aluminum alloys and prepared samples

Artificially corroded samples can more closely simulate actual in-service uniform corrosion than machined samples. Thus, in order to evaluate the eddy current technique's effectiveness in more realistic cases, two types of

corrosion samples were exposed to an accelerated corrosion test. The type-1 samples consisted of two separate plates, 40 and 61 mils thick, that were artificially corroded in a corrosion chamber until they reached about 5-10% thinning. The type-2 sample was created by fastening two 40 mil plates together with a rivet in each corner. This was also placed in a corrosion chamber with the expectation that trapped corrosion products between the layers would cause separation, thus closely simulating actual in-service corrosion.

The actual preparation of these specimens is described in more detail after the discussion below on the nature of corrosion in aluminum alloys.

3.4.2.1. General corrosion behaviour of Al Aluminum is a thermodynamically reactive material, as indicated by its position in the electromotive force (emf) series. However, it is very resistant to corrosion thanks to the barrier oxide film,  $\text{Al}_2\text{O}_3$ , that develops quickly in air and bonds strongly to the surface. In most cases the oxide film is stable and provides constant protection. However, in aqueous environments, the oxide layer can become hydrated and a more permeable  $\text{Al}_2\text{O}_3 \cdot 3\text{H}_2\text{O}$  film will develop. As shown by a Pourbaix diagram, Al is passive (protected by its oxide film) between a pH of about 4 to 8.5, the range of which depends on temperature and the presence of substances that can form soluble complexes or insoluble salts with aluminum. Beyond these limits, the aluminum oxides are soluble in many acids and bases, and the metal corrodes in these aqueous solutions in a general or uniform manner producing hydroxide,  $\text{Al}(\text{OH})_3$ , deposits [15]. In aircraft service environments, one faces NaCl and  $\text{SO}_2$  from sea water and engine exhaust, respectively, that can weaken the film while still in the passive

pH region. In these cases, combining either of these compounds with water as the electrolyte can initiate pitting corrosion in localized weak spots of the film. Pitting also begins when local galvanic cells initiate due to cathodic micro constituents such as  $\text{CuAl}_2$  in some copper-bearing aluminum alloys [16,17].

3.4.2.2. 2024 alloy corrosion The addition of copper to aluminum alloys always decreases corrosion resistance because of the large potential difference between the two metals. However, the nature and rate of corrosion depends on the amount of Cu added and the metallurgical treatment of the alloy. Al 2024's strength comes from aging after quenching, with the formation of coherent and semi-coherent metastable precipitates called  $\theta''$  and  $\theta'$  [18]. During this sequence, the stable  $\text{CuAl}_2$  phase,  $\theta$ , also forms and segregates to the grain boundaries. This creates a Cu depleted zone at the boundaries and sets up a galvanic cell due to the potential difference, resulting in intergranular corrosion, IGC. To forestall this, the alloy is clad with an Al 1230 alloy on both sides to a depth of 1.5 to 5% of the total thickness [17]. The more anodic cladding, called alclad, then acts as a sacrificial anode to protect the core 2024. Pits are usually the first form of corrosion to appear and they progress only as deep as the cladding.

3.4.2.3. Lap splices Moisture trapped between lap splice layers give rise to another electrochemical process called crevice corrosion. Water, chlorides and sulfides can accumulate and eventually reach levels that break down the protective film in localized weak spots between the layers. This results in pitting of the material between the layers under a passivation or film

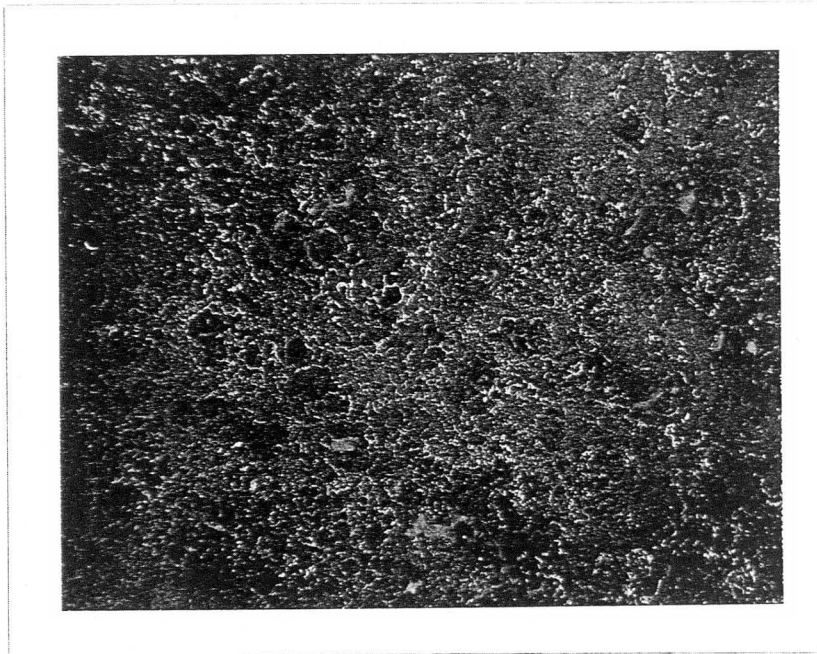
forming condition. The reactions cause the pH level to decrease within the pit cavities and increase in the oxygen rich areas outside the crevice where  $O_2$  is reduced to  $-OH$  [19]. A typical uniformly corroded aircraft lap splice has small areas up to several square inches of thinned material, usually around fasteners or near joint edges accompanied by some deep pits. The cladding in these areas dissolves first from a high concentration of shallow pits before the exposed core is attacked. In Al-Cu alloys, the  $Cu^{2+}$  cations, dissolved during the initial stage of corrosion, plate out onto the surface of the alloy and create many closely spaced cathodic sites. These sites promote further pitting due to the local cell reaction with the anodic pits; but, since many pits compete for these copper sites, most of them grow together uniformly. IGC may also take place laterally from the pit cavities, expediting further thinning especially in this cold rolled material with an elongated grain structure [16,17].

3.4.2.4. Type-1 sample preparation In order to simulate the rough pitted surface of corroded lap splices, two 2024-T3 aluminum alloy sheet samples were subjected to a corrosion chamber test given by a standard ASTM procedure [20], briefly described in appendix A. Prior to this test, each sample was masked to expose one large area as shown in Figure 3.6(b), then chemically treated to speed up the corrosion process in the chamber. This involved chemically milling off the cladding by dipping specimens into an NaOH solution of pH 13.9 at 95 °F for about one hour. About 2 mils were removed from each sample with this treatment. These were then placed in a corrosion chamber, the conditions of which are found in appendix A, until they developed appreciable uniform thinning after 40 days. The corrosion products

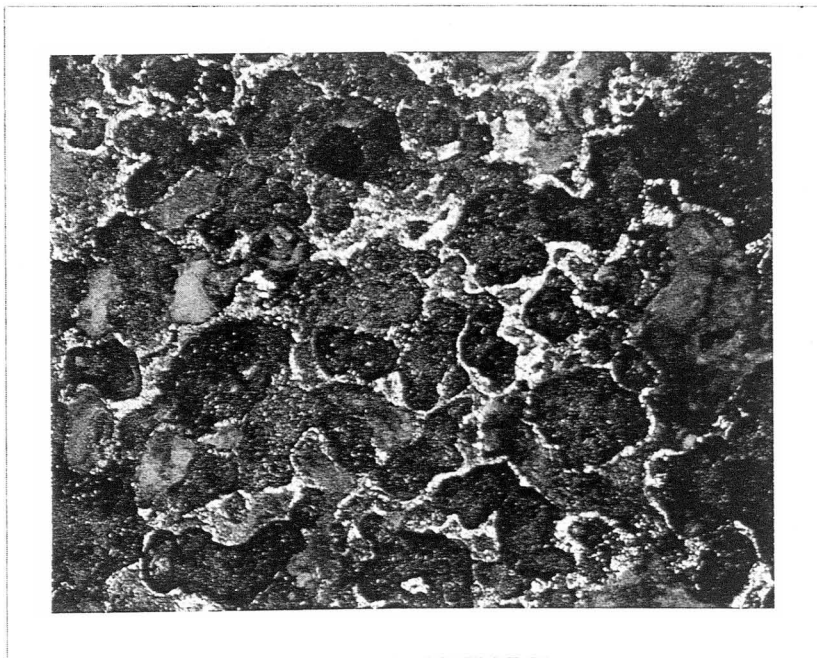
and salt deposits were removed from the corroded areas with HCl acid, and quickly cleaned with water to avoid any further deterioration from the acid.

3.4.2.5. Microscopic evaluation After removing the masking material, the samples were examined and measured for thinning with an optical microscope. The corroded metal surface exhibited a densely pitted texture as shown in the photos of Figure 3.8, at 4x and 40x magnification. Such a high density of shallow pits results in most of them joining to form much wider crevices that grow together. Although there are some significantly deep and narrow pits scattered sparsely throughout the corroded area, in general the result is a uniformly thinned sample at a macroscopic level. This is somewhat representative of real corrosion specimens, as depicted by Patton and Hsu [21]. They found that electrochemically corroded aluminum plates experienced generally uniform thinning with a roughness profile similar to that of a naturally corroded Boeing 727 sample with about 9% thinning when viewed as edge-on micrographs.

The microscope was also used to measure the actual average metal loss in both corrosion samples. The focusing knob is graduated with 2  $\mu\text{m}$  divisions. Thus, an accurate corrosion depth measurement can be found with respect to the top of the closest uncorroded area by measuring the difference in the knob's position between each focused area. This was done for nine spots in a 0.5"x0.5" area at the center of the 2"x2" corroded area, as shown in Figure 3.6(b). The average thinning depth was found for both samples in this manner. Since there also exists pits that are deeper and peaks that are higher than the mean thinning depth, only that position where the largest area of the rough surface is clearly in focus is used as the mean thinning depth at that



(a) Photo at 4x magnification



(b) Photo at 40x magnification

Figure 3.8 The artificially corroded surface of a 2024 -T3 alloy shown as (a) general corrosion, magnified 4x, and (b) the same area 40x to show the densely pitted surface

spot. This usually occurs within the widely joined pits and crevices. The resulting metal losses are given in Table 3.3. As with the machined samples, these will be measured with eddy current tests by pairing them with an uncorroded sample to simulate various locations of the corrosion.

Table 3.3. Corrosion samples' average metal thickness loss in inspection area shown in Figure 3.6(b)

Sample number	Plate thickness (mils)	Average metal loss (mils)
1b	61	4.5
2b	40	4.8

3.4.2.6. Type-2 sample preparation Actual in-service lap splices usually exhibit some plate separation since the corrosion product's specific volume is greater than that of the metal. This was simulated by exposing a lap splice sample to a corrosive environment. The sample consisted of two 2024-T3 plates fastened with one rivet near each corner. Before fastening, the plates were painted with zinc chromate, except for a 1.5 inch wide strip on the inside of the second layer. This was done to try to accelerate corrosion in one area between the layers. The sample was then painted white on the outside with an enamel paint, and placed into the chamber with the same environmental settings described in the appendix for about three months. Since it experienced negligible corrosion during this period, it was then subjected to a more aggressive treatment designed to initiate crevice and pitting corrosion and to remove part of the cladding. This involved

electrochemically etching the inner surface of the sample by placing it into a 0.025 M NaOH and KCl solution for two hours while making it anodic with respect to a platinum sheet using a current source, similar to the procedure described by Patton and Hsu [21]. Then the sample was returned to the corrosion chamber. The sample eventually displayed a pronounced amount of plate separation from the accumulation of corrosion products between the layers, called pillowing, after an additional five months in the chamber. This sample is considered a good representation of real in-service corrosion. The actual internal thinning is unknown; however, its location is probably within the unprotected 1.5 inch region in second layer. The separation is estimated at about 22 mils, deduced from the total outer thickness, and the paint thickness is 3 mils.

## CHAPTER 4. THEORY

### 4.1. Introduction to the Principles of Eddy Current Testing

The eddy current testing method is a form of electromagnetic nondestructive testing based on the principles of electromagnetic induction. The physical principles of eddy current testing are shown in Figure 4.1 [12]. The Maxwell-Ampere law states that an alternating current sets up a time varying magnetic field. When a primary coil excited with an alternating current is placed in close proximity to a conducting surface, the alternating primary magnetic fields from the probe interact with the surface and induce an emf in the material in accordance with the Maxwell-Faraday law. This induced voltage produces eddy currents in the material which, by Lenz's Law, set up secondary magnetic fields that oppose the ones producing them. The eddy currents, thus, are analogous to a mutually coupled secondary circuit in which the current flows in a circular direction opposite that of the current in the coil [12]. This mutual inductance causes a change in the impedance of the coil because the load of the secondary circuit, now the eddy currents in the specimen, are referred, or "reflected", back to the primary coil. For instance, the resistive component is a measure of the energy losses within the material since the eddy currents represent a resistive load. Hence, as a coil is brought close to a non-ferromagnetic conductive material its resistance, the real component of its impedance, increases.

Impedance also consists of a reactive imaginary component, called the inductive reactance. The work required to establish a magnetic flux in a coil,

or the energy stored in the magnetic field of a coil, is directly related to its inductance. Thus, when the opposing secondary field from the induced eddy currents decreases the magnetic flux linkages, as shown in Figure 4.1, the coil's stored energy decreases which in turn reduces its inductance and inductive reactance. However, when a coil with a certain magnetic field strength,  $H$ , is placed over a ferromagnetic material, the lower reluctance in the material allows the flux lines to increase in density within the coil's windings. This, therefore, increases the coil's inductance.

Any material property or geometry variances that affect the eddy currents' distribution and the related magnetic fields will always result in a change in the coil's impedance. These changes are monitored by either measuring them directly with an impedance analyzer or, more commonly, by

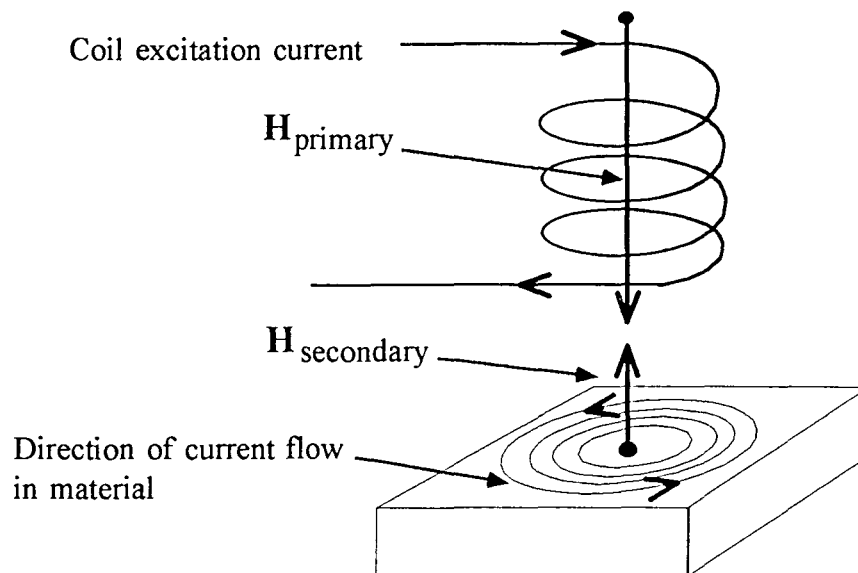


Figure 4.1: Principles of eddy current testing [12]

observing the trajectories traced on the scope of a commercial eddy current instrument. Usually, the signals are measured as departures from a reference condition, such as that for the coil placed on a standard specimen. Signals therefore result from changes in one or more of the specimen's properties such as conductivity, permeability, thickness, surface roughness, temperature and, most notably, the presence of defects. A defect, for example, deflects the eddy currents' path, especially if it is a crack perpendicular to the flow of the eddy currents, changing the secondary impedance, and hence the impedance of the coil. Test setup factors such as liftoff, frequency, and electronic noise also affect the signal. Under most operating conditions, the tests can differentiate between various factors and material properties if they each produce a different signal response. For example, commercial eddy scopes will display relatively distinctive trajectories for different types of defects. This allows the instrument to be setup in a way that separates an unwanted signal, such as that caused by liftoff, from the signal of interest, such as a flaw. Recorded signals can also be processed later by removing the noisy responses known to be caused by certain factors. Lastly, most eddy current instruments are equipped with electronic filters that reduce noise, especially that which occurs at high gain settings.

Commercial eddy current instruments are almost exclusively used to make relative measurements where reference standards are used to set the normal operating point. A material similar to the standard is tested by observing the signals that deviate from the reference condition; these indicate flaws or other property changes. A good understanding of these signals and how an instrument detects and displays them is necessary to develop a simple

calibration method that would make quantitative impedance measurements possible. Consequently, commercial instruments would be able to perform quantitative NDE, such as is now performed with an impedance analyzer in conjunction with an applicable eddy current theory.

#### 4.2. Theory of Eddy Current Phenomenon

Electromagnetic phenomena are governed by Maxwell's equations as follows: [22,14]

$$\nabla \times \mathbf{E} = -\frac{\partial \mathbf{B}}{\partial t} \quad (4.1)$$

$$\nabla \times \mathbf{H} = \mathbf{J} + \frac{\partial \mathbf{D}}{\partial t} \quad (4.2)$$

$$\nabla \cdot \mathbf{B} = 0 \quad (4.3)$$

$$\nabla \cdot \mathbf{D} = \rho \quad (4.4)$$

The constitutive relations for an isotropic, linear and homogeneous medium are given as

$$\mathbf{B} = \mu \mathbf{H} \quad (4.5)$$

$$\mathbf{D} = \varepsilon \mathbf{E} \quad (4.6)$$

$$\mathbf{J} = \sigma \mathbf{E} \quad (4.7)$$

where

$\mu$  = the magnetic permeability in henrys per meter (H/m)

$\varepsilon$  = the electric permittivity in farads per meter (F/m), and

$\sigma$  = the electric conductivity in siemens per meter (S/m).

Since the divergence of  $\mathbf{B}$  is zero from equation (4.3),  $\mathbf{B}$  can be expressed as the curl of another vector, called the magnetic vector potential  $\mathbf{A}$ , given by

$$\mathbf{B} = \nabla \times \mathbf{A} . \quad (4.8)$$

Combining this with equation (4.1) gives

$$\nabla \times \mathbf{E} = -\nabla \times \frac{\partial \mathbf{A}}{\partial t} \quad (4.9)$$

or

$$\nabla \times \left( \mathbf{E} + \frac{\partial \mathbf{A}}{\partial t} \right) = 0 . \quad (4.10)$$

Since an irrotational field can be replaced with the gradient of a scalar potential function, the solution to equation (4.10) is

$$\mathbf{E} + \frac{\partial \mathbf{A}}{\partial t} = -\nabla V \quad (4.11)$$

where  $V$  is the scalar electric potential.

Now, substituting equation (4.5) into equation (4.2) yields

$$\nabla \times \mathbf{B} = \mu \left( \mathbf{J} + \frac{\partial \mathbf{D}}{\partial t} \right) \quad (4.12)$$

The displacement current  $\frac{\partial \mathbf{D}}{\partial t}$  is negligible when compared to the total current density,  $\mathbf{J}$ , for the relatively low operating frequencies in eddy current testing

(below 10 MHz). This is called the quasi static approximation. Therefore, combining equations (4.7), (4.8) and (4.12) we have

$$\nabla \times \nabla \times \mathbf{A} = \mu \mathbf{J} \quad (4.13)$$

$$= \mu \sigma \mathbf{E} . \quad (4.14)$$

Replacing  $\mathbf{E}$  in equation (4.14) with the relation of (4.11) gives

$$\nabla \times \nabla \times \mathbf{A} = \mu \sigma \left( -\nabla V - \frac{\partial \mathbf{A}}{\partial t} \right) . \quad (4.15)$$

Recognizing the vector identity

$$\nabla \times (\nabla \times \mathbf{A}) = \nabla (\nabla \cdot \mathbf{A}) - \nabla^2 \mathbf{A} \quad (4.16)$$

and choosing the Coulomb gauge  $\nabla \cdot \mathbf{A} = 0$ , equation (4.15) becomes the following partial differential equation for any time varying current [22]

$$\nabla^2 \mathbf{A} = -\mu \mathbf{J}_s + \mu \sigma \frac{\partial \mathbf{A}}{\partial t} \quad (4.17)$$

where  $\mathbf{J}_s = -\sigma \nabla V$  is the source current density in amperes per square meter, such as an infinite sheet of current over a conductive half-space. Assuming the fields are time harmonic and vary sinusoidally in steady state, sinusoidal eddy currents will exist within the conductor and  $\mathbf{A}$  can be expressed as

$$\mathbf{A} = \mathbf{A}_m e^{j\omega t} \quad (4.18)$$

where  $\omega$  is the angular frequency and  $j$  is the notation used to define a complex number, where  $j = \sqrt{-1}$ . Differentiating with respect to time, we get

$$\frac{\partial \mathbf{A}}{\partial t} = j\omega \mathbf{A} \quad (4.19)$$

Thus, substituting equation (4.19) into (4.17) results in [22]

$$\nabla^2 \mathbf{A} = j\omega\mu\sigma \mathbf{A} - \mu \mathbf{J}_s \quad (4.20)$$

where the first term is a function of the density of the induced eddy currents,  $\mathbf{J}_e$ , given by

$$\mathbf{J}_e = j\omega\sigma \mathbf{A} \quad (4.21)$$

The ability to obtain analytic solutions for the magnetic vector potential from equation (4.20) is usually limited to simple geometries such as a symmetrical coil over an infinite half space medium. This equation also governs the skin effect that will be discussed in the next section.

### 4.3. Skin Effect

Equation (4.17) is a diffusion equation that describes the propagation of EM fields in a conductor. Assuming an exciting current sheet is flowing in the x direction over a conducting half-space, the magnetic field intensity,  $H_y$ , in the conductor as a function of depth from the surface,  $z$ , is found to be [14]

$$\mathbf{H}_y = \mathbf{H}_0 e^{\left[-z\left(\frac{\omega\mu\sigma}{2}\right)^{1/2}\right]} e^{\left[-jz\left(\frac{\omega\mu\sigma}{2}\right)^{1/2}\right]} \quad (4.22)$$

Hence, EM fields decay exponentially with depth. This effect also applies to eddy currents, where the induced current density,  $\mathbf{J}_e$ , is given by

$$\mathbf{J}_e = \mathbf{J}_0 e^{-z/\delta} e^{-jz/\delta} \quad (4.23)$$

where

$$\delta = \left( \frac{2}{\omega \mu \sigma} \right)^{1/2} \quad (4.24)$$

is skin depth or standard depth of penetration. This is the depth at which the magnitude of the induced eddy current density decreases by a factor of  $1/e$  from its value at the surface,  $\mathbf{J}_0$ . This current distribution is illustrated in Figure 4.2 [12]. The eddy currents are confined to a thin layer of the conductor's surface adjacent to the coil, and relationship (4.23) indicates that lower frequencies are required to reach greater depths and detect or measure deeper subsurface flaws.

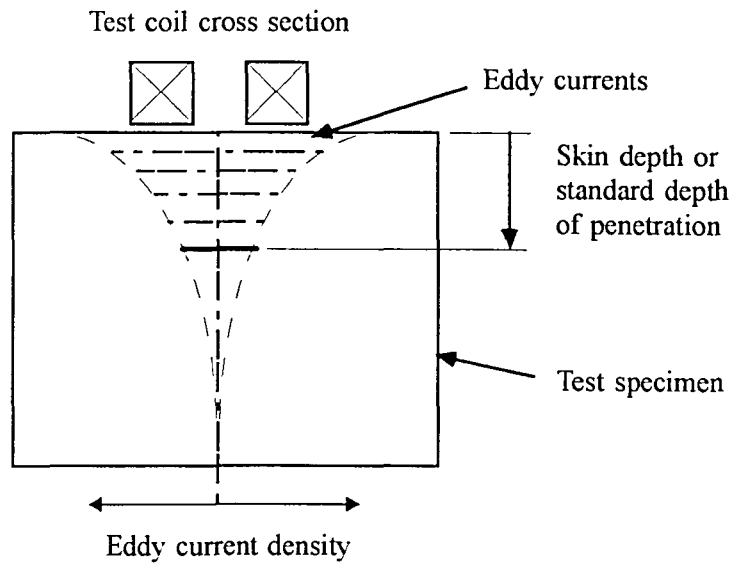


Figure 4.2: Skin Effect [12]

#### 4.4. Forward Solution for the Impedance of a Coil Over a Multi-Layered Half-Space

With the principles and fundamental equations of eddy current phenomena now known, the model for the impedance of a coil in a given situation can be better understood. Uzal and Moulder [1] adapt the Cheng, Dodd and Deeds' forward solution for the impedance of an air-core coil placed over an arbitrary number of planar, non-ferromagnetic, conducting layers [3] to the four layer geometry depicted in Figure 4.3(a). This represents a corroded lap splice where region 1 (the substrate layer or the infinite half-space) and region 3 consist of air and regions 2 and 4 are 2024-T3 alloy skin material. The regions above  $z=0$  are assumed to have the properties of air. The permeability is taken as that of free space,  $\mu_0$ , for all regions.

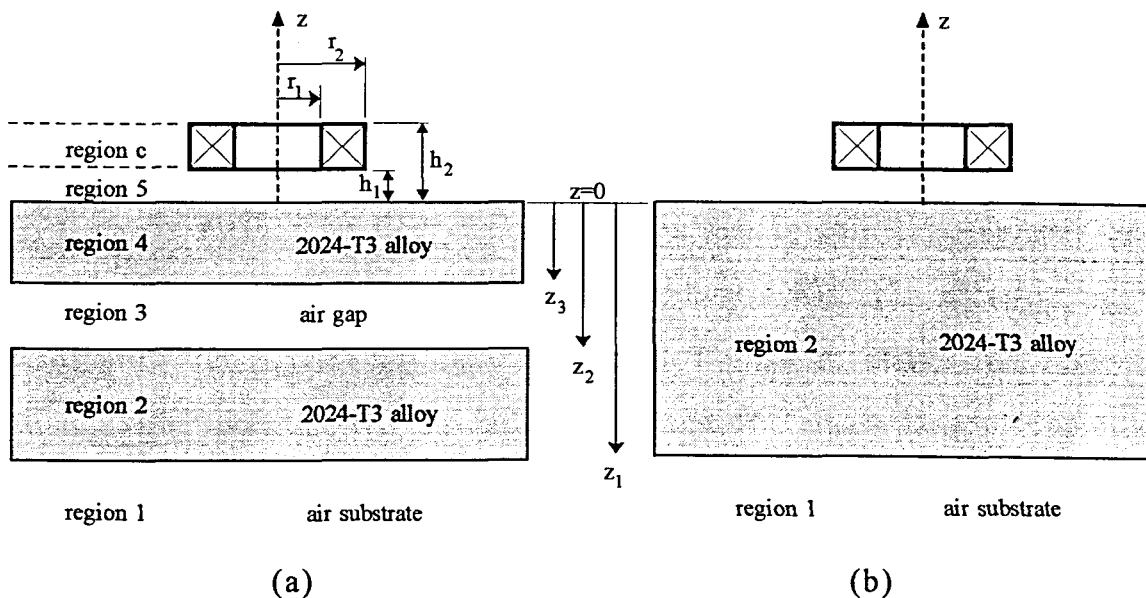


Figure 4.3: Theoretical model of the coil over a (a) four layered half space; air gap represents thinning in a lap splice, and (b) two layered half space for the uncorroded measurement

The solution assumes time harmonic eddy currents are produced in linear, isotropic and homogeneous media with a geometry that is symmetrical about the axis of the coil inducing the currents. This implies materials for which  $\sigma$  does not vary in the region being considered and uniform thickness in all layers. This geometry simplifies the solution for the magnetic vector potential defined by the differential equation (4.20) derived in section 4.2. Also, the geometry is assumed symmetrical about the coil's z-axis so that  $\mathbf{A}$  only has a  $\theta$  component and equation (4.20) is solved in cylindrical coordinates  $(r, \theta, z)$ .

The general procedure consists of first treating the coil as a single loop delta function coil and performing a separation of variables on the vector potential's differential equation, obtaining a separation constant,  $\alpha$ . The coefficients for the  $\mathbf{A}(r, z)$  solutions are then found from boundary conditions for the fields at the interfaces, which each vary with  $\alpha$ . Since  $\alpha$  is a continuous variable the complete solution is the integral of the primitive solution over the complete range of  $\alpha$  from 0 to infinity. Uzal and Moulder [1] use a matrix method to find the coefficients due to the large number linear equations generated in this multi-layer problem. With the solution for the vector potential  $\mathbf{A}_n(r, z)$  now known in each region,  $n$ , above and below the coil and within each layer, the induced voltage of a single loop pickup coil in any region is

$$\mathbf{V}(r, z) = -\oint \mathbf{E} \cdot d\mathbf{l} \quad (4.25)$$

$$= j\omega 2\pi \mathbf{A}_n(r, z) \cdot \quad (4.26)$$

Now, the self-induced voltage can be found for a coil, which is both the driver and pickup coil, by integrating the vector potential  $\mathbf{A}_c(r,z)$  within the coil's region ( $n=c$  in Figure 4.3) over the coil's cross sectional area, giving

$$\mathbf{V}(r,z) = \frac{j2\pi\omega n}{(h_2 - h_1)(r_2 - r_1)} \int_{h_1}^{h_2} \int_{r_1}^{r_2} r \mathbf{A}_c(r,z) dr dz \quad (4.27)$$

assuming the coil is uniformly wound with  $n$  turns. The coil's impedance is found by dividing the voltage of equation (4.27) by the applied current,  $I$ , in the coil. Hence,

$$Z = K \int_0^\infty \frac{I^2(\alpha)}{\alpha^5} \left\{ 2L + \frac{1}{\alpha} \left[ 2e^{-\alpha L} - 2 + (e^{-\alpha h_1} - e^{-\alpha h_2})^2 \frac{U_{12}}{U_{22}} \right] \right\} d\alpha \quad (4.28)$$

where  $U_{12}$  and  $U_{22}$  represent the second column of the 2 by 2 matrix that is the product of

$$\mathbf{U} = \mathbf{T}_{5,4} \mathbf{T}_{4,3} \mathbf{T}_{3,2} \mathbf{T}_{2,1} \quad (4.29)$$

where

$$\mathbf{T}_{k+1,k} = \frac{1}{2} \begin{bmatrix} (1 + \beta_k) e^{(\alpha_{k+1} - \alpha_k) z_k} & (1 - \beta_k) e^{(\alpha_{k+1} + \alpha_k) z_k} \\ (1 - \beta_k) e^{-(\alpha_{k+1} + \alpha_k) z_k} & (1 + \beta_k) e^{-(\alpha_{k+1} - \alpha_k) z_k} \end{bmatrix} \quad (4.30)$$

and

$$\alpha_k = \sqrt{\alpha^2 + j\omega\mu_0\sigma_k} \quad (4.31)$$

$$\beta_k = \frac{\alpha_k}{\alpha_{k+1}} \quad (4.32)$$

Each T matrix represents the relations between  $A_c(r,z)$ 's coefficients of two neighboring layers, k and k+1, where k=1,2,3,4 in this four layer case. The length of the coil is  $L=h_2-h_1$  and the prefactor of equation (4.27) is given by

$$K = \frac{\pi n^2 j \omega \mu_o}{L^2 (r_2 - r_1)^2} \quad (4.33)$$

and

$$I(\alpha) = \int_{r_1 \alpha}^{r_2 \alpha} x J_1(x) dx \quad (4.34)$$

where  $J_1$  is a first order Bessel function. Experimental eddy current tests are usually performed by taking the difference in impedance between two measurements, with one of them as a reference for the flawless or null case. Therefore, the measured quantity due to the material loss in a lap splice shown in Figure 4.3 is

$$\Delta Z = Z' - Z \quad (4.35)$$

where  $Z'$  is the coil impedance over the uncorroded material. Thus, the coil's theoretical impedance change is needed to facilitate comparison to experiment. The subtraction also reduces errors due to imperfect modeling of the coil.

Figure 4.3(b) shows the uncorroded lap splice as a simple two layer geometry. The impedance for this case can be computed in a manner similar to the above. The impedance change is thus given by

$$\Delta Z = K \int_0^{\infty} \frac{I^2(\alpha)}{\alpha^6} (e^{-\alpha h_1} - e^{-\alpha h_2})^2 \left\{ \frac{(\alpha + \alpha_2)(\alpha_2 - \alpha_1) + (\alpha - \alpha_2)(\alpha_2 + \alpha_1)e^{-2z_1\alpha_2}}{(\alpha - \alpha_2)(\alpha_2 + \alpha_1) + (\alpha + \alpha_2)(\alpha_2 - \alpha_1)e^{-2z_1\alpha_2}} - \frac{U_{12}}{U_{22}} \right\} d\alpha . \quad (4.36)$$

Those terms that were associated with the impedance of the coil in air have canceled out.

It should be noted that the term "air gap" refers to the amount of thinning, even when it is on the bottom of the second layer where it may not seem as obvious. In this specific case, the corroded area also consists of only 2 layers, with the top metal layer simply being thinner than in the uncorroded case.

#### 4.5. Swept Frequency Analysis of Corroded Lap Splices

As mentioned in chapter 2, the theoretical value for both the real and imaginary components of  $\Delta Z$  can be plotted vs. frequency to show some of the characteristics of these curves with respect to layer thicknesses. Equation (4.36) was used to model coil ISU 2, with the parameters given in Table 3.1, over two 40 mil thick 2024-T3 alloy plates with flat-bottomed holes, with diameters greater than the coil, that simulate thinning in a lap splice due to corrosion. This thinning was modeled at the four different locations shown in Figure 3.7.

The theoretical frequency response of a coil's change in resistance,  $\Delta R$ , for various example amounts of thinning and locations are given in Figures 4.4 to 4.7. Note that a minimum exists in every  $\Delta R$  vs. frequency curve. The air gap location, as well as the amount of metal loss, has a definite effect on the frequency and the magnitude of the minimum,  $\Delta R_{\min}$ . In general, the response

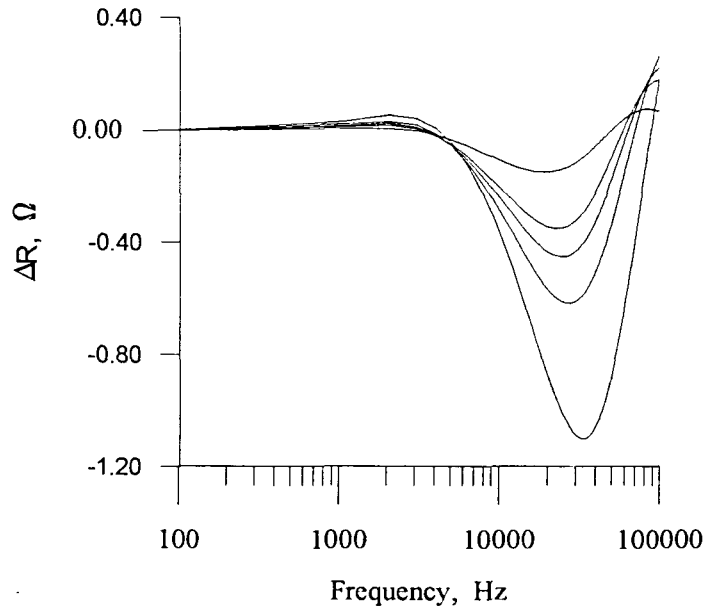


Figure 4.4: Theoretical swept frequency data for first layer thinning

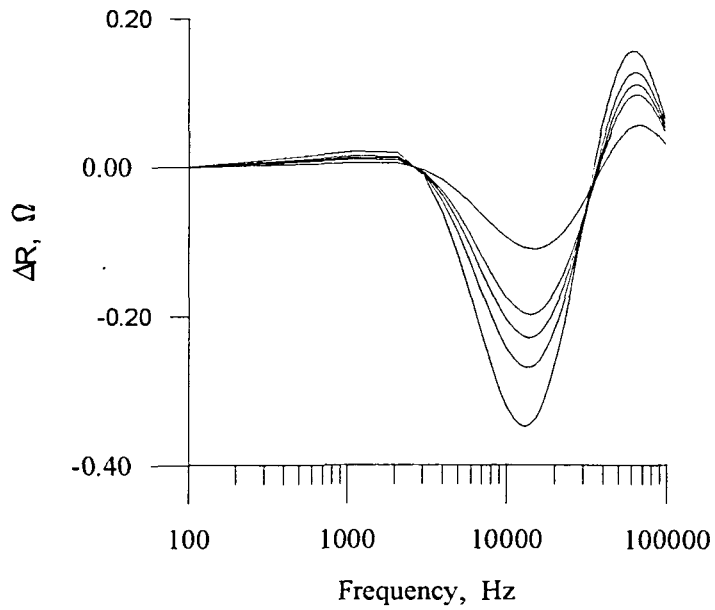


Figure 4.5: Theoretical swept frequency data for second layer thinning

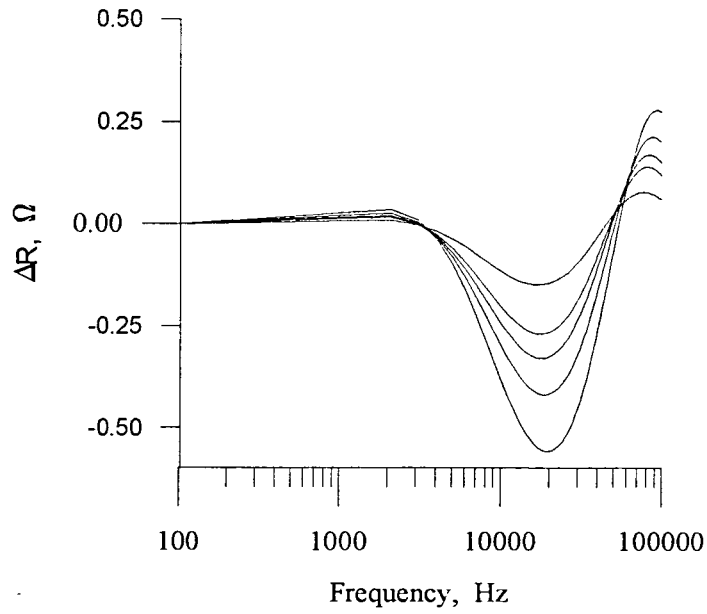


Figure 4.6: Theoretical swept frequency data for thinning in both layers

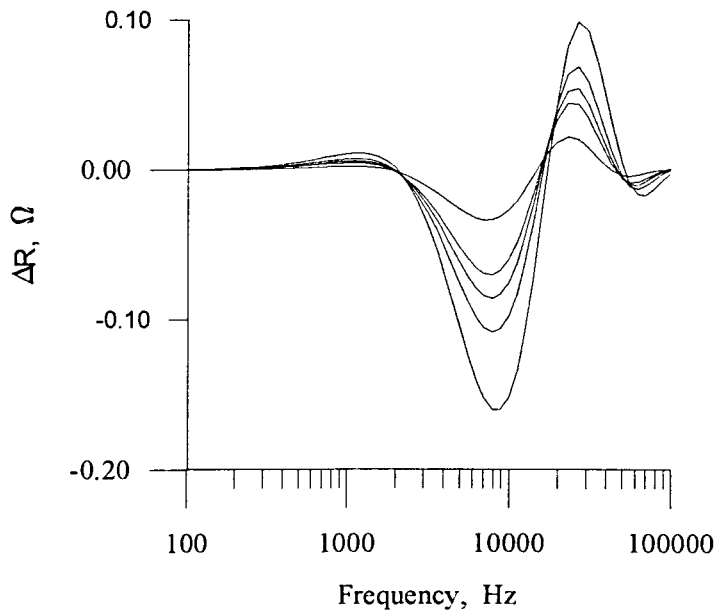


Figure 4.7: Theoretical swept frequency data for thinning on the bottom surface

starts from zero at zero frequency, and increases slightly until it quickly drops across the zero to form a minimum, then increases and eventually crosses the zero axis again before reaching a maximum. The five curves in each figure represent the responses for five different air gap thicknesses, namely: 4, 8, 10, 12 and 16 mils. The curves with the deepest minima correspond to those samples with the most metal loss (or air gap). However, Figure 4.8 shows the effect of the four different thinning locations on the frequency of the minimum for an air gap 8 mils thick. It is clear that the farther away the air gap is from the surface with the probe, the lower the frequency at which the minimum  $\Delta R$  occurs. Also, the signal is weaker for those deeper locations.

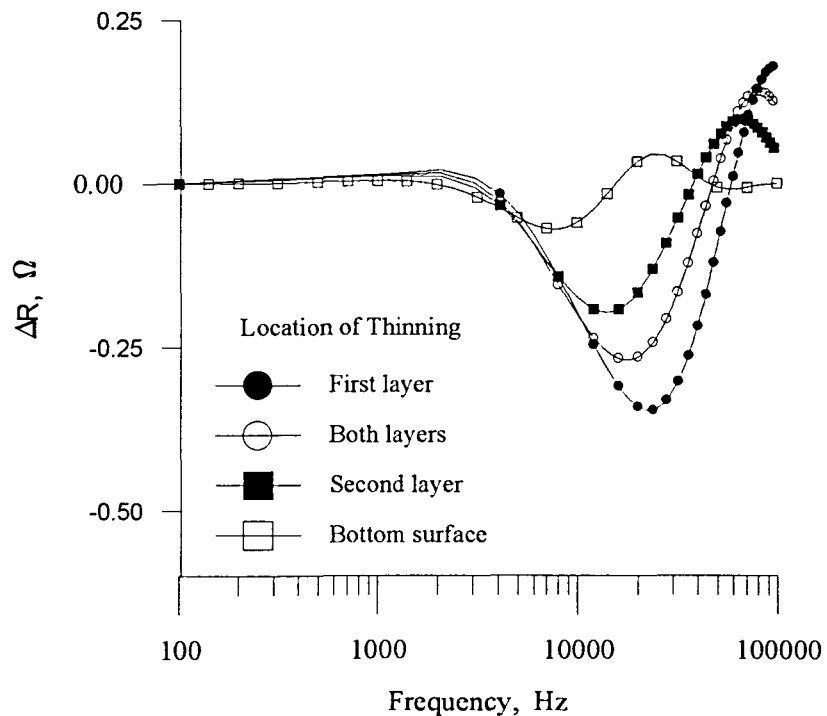


Figure 4.8: Frequency shift of the minimum affected by the location of an 8 mil thinned region

The shift in the minimum makes physical sense considering that the skin depth increases with decreasing frequency, thus allowing the eddy currents to reach and detect the material loss in the second layer, even at the bottom of the lower plate. Also, this kind of frequency shift occurs as the amount of thinning changes when it is located in the first layer, as shown in Figure 4.4. But, no such shift is evident for second layer thinning of Figure 4.5 or 4.7. A more detailed discussion is given in chapter 6 when these theoretical results are compared to experimental curves.

#### 4.6. Inversion Procedure

With the forward solution well defined, swept frequency experimental measurements of the coil's impedance change can be inverted using the theory to determine the thickness of the three layers in Figure 4.3. However, an analytic inversion of the very complex impedance difference equation (4.36) is unlikely [3]. Since the coil parameters and the conductivities for both air and the metal 2024-T3 are known, the inversion method need only infer the three layer thicknesses in Figure 4.3. In principle, the three interface locations are given by

$$z_1 = -c_1 - c_2 - c_3$$

$$z_2 = -c_1 - c_2$$

$$z_3 = -c_1$$

where the thicknesses are  $c_1$  for the top layer,  $c_2$  for the air gap, and  $c_3$  for the bottom layer, and the air substrate goes to infinity. As described by Moulder *et al.* [9], a least-squares method is used, defining a cost function as follows:

$$Q \equiv \sum_{k=1}^N \left( \left| \Delta R_{\text{exp}}(\omega_k) \right| - \left| \Delta R_{\text{theory}}(\omega_k, c_1, c_2, c_3) \right| \right)^2. \quad (4.37)$$

This function is minimized by using a simplex direct search method that repeatedly solves for the frequency dependence of  $\Delta R$  from equation (4.36) while changing the three layer thicknesses to find the theory curve that best matches the experimental data. This is typically accomplished with 100 iterations while minimizing the cost function for  $N=20$  frequencies using a computer program.

Note that this method always assumes the three unknown layers are in the metal-air-metal order shown in Figure 4.3. Hence, the inversions given in this thesis are limited only to those cases where the corrosion is located between the layers and not at the bottom of the second layer. However, by giving the inversion algorithm the initial total thickness of the two uncorroded metal layers, and keeping it constant, the procedure can theoretically account for plate separation as well as determine the location of the thinning without their initial knowledge.

#### 4.7. Commercial Eddy Current Instruments and Test Coil Signals

In this section, we explore the relationship between the test coil signals and their representation and detection via a generic eddy current instrument. An eddy current test coil behaves like a transformer in that the test specimen impedance is referred into the coil through magnetic coupling, as shown in Figure 4.1. A circuit representation of this electromagnetic test is illustrated in Figure 4.9(a), where the secondary circuit replaces the specimen being

tested. Given a constant current source,  $I_p$ , and a variable resistor,  $R_s$ , the resulting voltage signals can be represented by the phasor diagram in Figure 4.9(b). Phasors and phasor diagrams are useful when analyzing sinusoidal, time-domain functions such as the voltage and current of AC circuits used in eddy current tests. Given a constant frequency, the phasor is a vector with a length equal to the RMS signal amplitude and an angular phase angle depicting the lead or lag with respect to a reference signal. The RMS voltage and current phasors are symbolized with bold capital letters  $V$  and  $I$ . The horizontal axis is used as the zero angle or in-phase reference and can be considered as the direction that describes the signals that are in phase with the reference signal, which in this case is the driving alternating current source,  $I_p$ . The total voltage drop across the primary coil,  $V_p$ , is given by the phasor  $OA$  for an open secondary circuit, or  $R_s = \infty$ . This is analogous to the test coil in air. This phasor is decomposed into a vertical and horizontal component consisting of the voltage across the coil with inductance  $L_p$  and resistance  $R_p$  respectively. The current is said to lag the total voltage,  $V_p$ . Solution of the circuit equations for Figure 4.9(a) shows that, as the secondary resistance,  $R_s$ , decreases, the total voltage drop decreases and rotates towards the in-phase position with the current. The resulting locus is a semicircle as  $R_s$  varies from  $\infty$  to 0, as shown in Figure 4.9(b). When an eddy current probe is placed on a conducting half-space, a similar locus would occur if the conductivity of a specimen could be continuously increased. Hence, phasor  $OB$  denotes the signal for the coil on a metal with a certain resistance (or conductance) [14].

Phasor diagrams are especially useful in representing the signals in compensating or null balance circuits. Since all signals are relative, they can

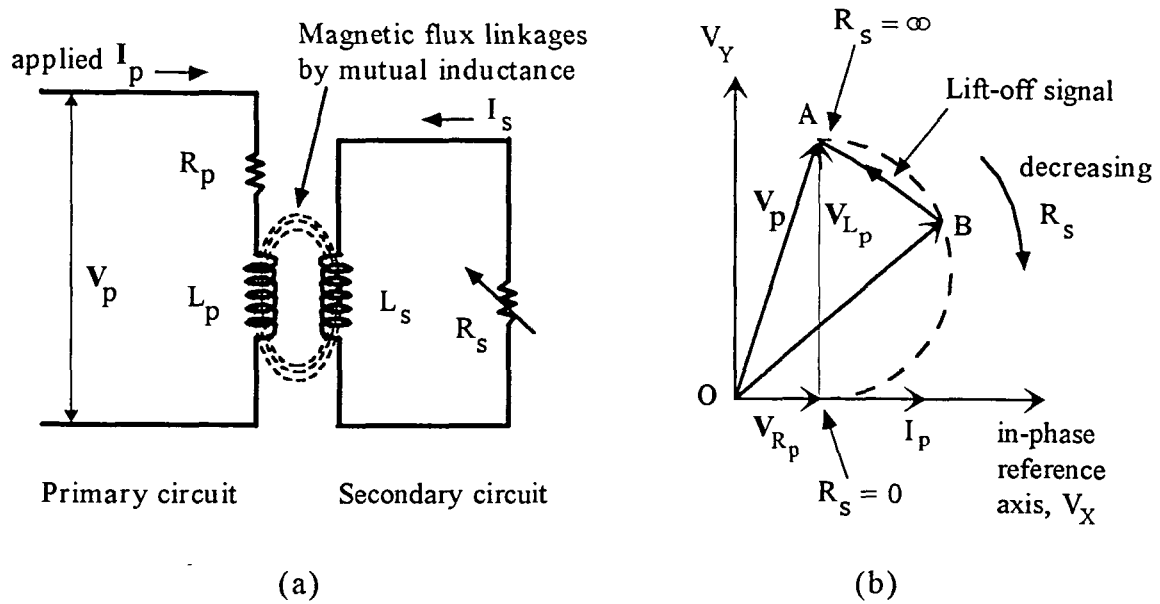


Figure 4.9: Electromagnetic test represented as (a) an air-cored transformer, and (b) its phasor diagram

be viewed from any reference point, not just the origin at  $O$ . For example, if the normal test object's operating point is given by the test coil output signal  $OB$ , it can be brought to the null condition by adding its negative signal  $-OB$  [14]. Now, any new signals are represented by phasors drawn from the new reference point, at the null, to the head of the signal. Lift-off would therefore draw a trajectory from point  $B$  towards  $A$  as shown in Figure 4.9(b). An eddy current instrument basically functions in this manner and uses electronic circuits to perform the null operation. The screen displays the voltage vectors as phasors that represent the amplitudes and phase angles of the signals viewed from the null position.

If an eddy current instrument can be modeled by the simple circuit in Figure 4.9(a) with a constant current source as depicted above, the resulting voltage drop  $V_P$  is directly proportional to the electrical impedance of the coil. Thus, the phasor diagram in Figure 4.9(b) can also represent the impedance of the coil in a complex plane, with the horizontal axis as the resistance and the vertical as the reactance. In contrast, most eddy current instruments use test coils driven by a constant voltage source,  $V_S$ , rather than a current source. Also, the display on the instruments' screen and analog output are given as horizontal and vertical voltages. However, the in-phase reference axis is not necessarily horizontal since the orientation angle is variable and selected by the user. Thus the output voltage components,  $V_H$  and  $V_V$ , do not necessarily correspond to the actual test coil signal's in-phase ( $0^\circ$ ) and quadrature ( $90^\circ$ ) components, which would lie in the  $V_X$  and  $V_Y$  axes respectively. These, in turn, do not correspond to the impedance plane, as is arbitrarily shown in Figure 4.10.

Since the probes are connected in a differential configuration, the output voltage can be modeled as a signal across a bridge circuit, as illustrated in Figure 4.11. This circuit is a simplified model of an eddy current instrument that can easily be dealt with by circuit analysis to give sufficiently representative results. The reference coil has an inductance and resistance of  $L_1$  and  $R_1$  respectively; similarly, the test coil's values are  $L_2$  and  $R_2$ . The voltage drop across each coil is  $V_1$  and  $V_2$  and the output voltage across the bridge is  $V_0$ . The instrument's input impedance is given by two equivalent resistances,  $R_0$ . A relationship between  $\Delta Z$  and  $\Delta V$  can be found from circuit analysis, after which the effects of introducing a small perturbation or change

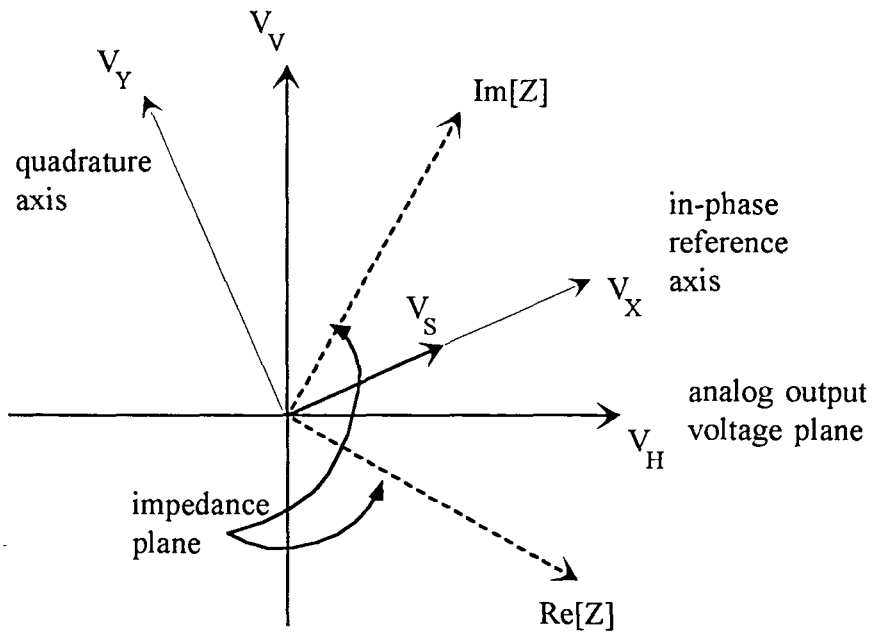


Figure 4.10: Output signal coordinate systems

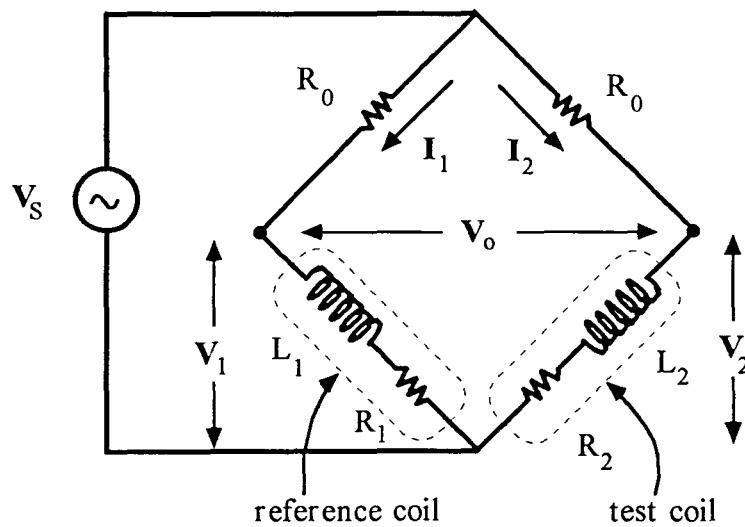


Figure 4.11: Bridge circuit modeling an instrument connected to a probe

in the coil's resistance,  $dR_2$  can be analyzed. Note that the impedance,  $Z$ , is a complex number, not a phasor, because it has no corresponding sinusoidal time-domain function of any physical meaning. The current in the reference coil is given by

$$\mathbf{I}_1 = \frac{\mathbf{V}_s}{R_0 + j\omega L_1 + R_1} \quad (4.38)$$

and the voltage drop, by

$$\mathbf{V}_1 = \mathbf{I}_1 (j\omega L_1 + R_1) \quad (4.39)$$

$$\mathbf{V}_1 = \frac{\mathbf{V}_s (j\omega L_1 + R_1)}{(R_0 + j\omega L_1 + R_1)} \quad (4.40)$$

Rearranging equation (4.40) and multiplying top and bottom by the complex conjugate of the denominator, we get

$$\frac{\mathbf{V}_1}{\mathbf{V}_s} = \frac{(j\omega L_1 + R_1)(R_0 + R_1 - j\omega L_1)}{(R_0 + R_1)^2 + (\omega L_1)^2} \quad (4.41)$$

$$= \frac{R_0 R_1 + R_1^2 + (\omega L_1)^2 + j\omega L_1 R_0}{(R_0 + R_1)^2 + (\omega L_1)^2} \quad (4.42)$$

Similarly, the test coil's voltage drop is given by

$$\frac{\mathbf{V}_2}{\mathbf{V}_s} = \frac{R_0 R_2 + R_2^2 + (\omega L_2)^2 + j\omega L_2 R_0}{(R_0 + R_2)^2 + (\omega L_2)^2} \quad (4.43)$$

By inspection of the circuit we have

$$\frac{\mathbf{V}_o}{\mathbf{V}_s} = \frac{\mathbf{V}_1}{\mathbf{V}_s} - \frac{\mathbf{V}_2}{\mathbf{V}_s} \quad (4.44)$$

Therefore, by substitution, the resulting output voltage is given by

$$\frac{V_o}{V_s} = \left[ \frac{R_0 R_1 + R_1^2 + (\omega L_1)^2}{(R_0 + R_1)^2 + (\omega L_1)^2} - \frac{R_0 R_2 + R_2^2 + (\omega L_2)^2}{(R_0 + R_2)^2 + (\omega L_2)^2} \right] + j \left[ \frac{\omega L_1 R_0}{(R_0 + R_1)^2 + (\omega L_1)^2} - \frac{\omega L_2 R_0}{(R_0 + R_2)^2 + (\omega L_2)^2} \right]. \quad (4.45)$$

Now, assuming all quantities are constant except for  $R_2$ , the output voltage ratio can be expressed as

$$\frac{V_o}{V_s} = f(R_2). \quad (4.46)$$

Expanding this function in a Taylor series about  $R_2 = R_2^0 + dR_2$  gives

$$f(R_2) = f(R_2^0) + f'(R_2^0)[R_2 - R_2^0] + \left\{ \frac{f''(R_2^0)}{2!}[R_2 - R_2^0]^2 + \frac{f'''(R_2^0)}{3!}[R_2 - R_2^0]^3 \dots \right\} \quad (4.47)$$

where  $R_2^0$  is the initial value of the test coil's resistance and the higher order terms in the curly brackets are neglected for small perturbations,  $dR_2$ . Substituting the term in the square brackets for  $dR_2$  and using equation (4.46) simplifies the expression to

$$f(R_2) = \frac{V_o}{V_s} \Big|_{R_2^0} + \frac{\partial \left( \frac{V_o}{V_s} \right)_{R_2^0}}{\partial R_2} dR_2. \quad (4.48)$$

Assuming the eddy current instrument is nulled before adding a pure  $dR_2$  signal, any output signal  $f(R_2)$  for  $dR_2=0$  that imbalances the bridge is subtracted and the resulting measured signal,  $\Delta V_o$ , is a function of  $dR_2$  only.

Thus, we have

$$\Delta V_o = f(dR_2) \quad (4.49)$$

where

$$f(dR_2) = f(R_2)_{dR_2 \neq 0} - f(R_2)_{dR_2 = 0} \quad (4.50)$$

$$= \frac{\partial \left( \frac{V_o}{V_s} \right)_{R_2^0}}{\partial R_2} dR_2 \quad (4.51)$$

Now, partially differentiating the bridge transfer function of equation (4.45) with respect to  $R_2$  yields

$$\frac{\partial \left( \frac{V_o}{V_s} \right)}{\partial R_2} = \left\{ \frac{\left[ (R_0 + R_2)^2 + (\omega L_2)^2 \right] (R_0 + 2R_2) - \left[ (R_0 + R_2)R_2 + (\omega L_2)^2 \right] 2(R_0 + R_2)}{\left[ (R_0 + R_2)^2 + (\omega L_2)^2 \right]^2} - j \left\{ \frac{-2(R_0 + R_2)\omega L_2 R_0}{\left[ (R_0 + R_2)^2 + (\omega L_2)^2 \right]^2} \right\} \right\} \quad (4.52)$$

and substituting this result into equation (4.51) produces the output signal

$$f(dR_2) = \left\{ \frac{\left( R_0 \omega^2 L_2^2 - R_0^3 - 2R_0^2 R_2^0 - R_0 R_2^{0^2} \right) + j2\omega L_2 R_0 (R_0 + R_2^0)}{\left[ (R_0 + R_2^0)^2 + (\omega L_2)^2 \right]^2} \right\} dR_2 \quad (4.53)$$

The small resistance changes,  $dR_2$ , can be provided by various small resistors inserted in series with the test coil and their values can be expressed as  $\Delta R_2$ . Since equation (4.53) represents the change in output voltage,  $\Delta V_o$ , due to a small change in the test coil resistance, it is evident that the term

inside the curly brackets is an expression for the ratio  $\Delta V_0$  divided by  $\Delta R_2$ . The relationship  $\Delta V_0/\Delta R_2$ , that we shall call a calibration factor with units of  $V/\Omega$ , is constant for a given frequency. Since this factor was found with the provision that the probe's inductances and other resistances remain unchanged, its magnitude must be found experimentally with the probe consistently positioned over a specific normal test specimen. Hence, the calibration factor is valid only for that specific instrument-probe-material combination. Small changes in the coil's inductance due to flaws, minor conductivity or thickness variances will not appreciably affect the calibration factor.

Equation (4.53) reveals that, in principle, the calibration factor is a complex function, the components of which can be expressed in the phasor domain. The small pure resistive changes produce signals that define the real axis of the impedance plane, located at some angle from the instrument's in-phase reference axis,  $V_X$ , as shown in Figure 4.10. Note that these reference axes are arbitrarily located with respect to the instrument's analog voltage output signals,  $V_H$  and  $V_V$ . The in-phase component of  $\Delta V_0$  lies in  $V_X$ , not  $V_H$ .

In practice we can disregard the complex relationship and the location of  $V_X$ , and use the fact that the signal's total magnitude  $|\Delta V_0|$  is directly proportional to the resistance change  $|\Delta R_2|$  to obtain a simple constant for the calibration factor. Also, by keeping the same angle setting on the instrument, the impedance plane's angular position will be constant on the instrument's screen at a given frequency. Thus, that angular position can be referenced in terms of the output voltage components,  $V_H$  and  $V_V$ . Now, any signal due to a flaw will have an orientation within the impedance plane that consists of a

resistive and reactive component. The resistive component has already been related to the voltage signal output by means of the calibration factor; hence, the reactive part,  $\Delta X_{L_2}$ , can in turn be determined by relating it to the resistive component's orientation and magnitude.

An impedance plane's imaginary (reactive) axis is given by the line leading the real axis by  $90^\circ$ . This orthogonality for a calibrated instrument can be verified analytically with the same approach as before, but for changing  $dL_2$ . While avoiding a repeat of the previous analysis, the output voltage signal  $\Delta V_o$  is given by

$$\frac{V_o}{V_s} = f(L_2) \quad (4.54)$$

assuming all quantities are constant except for  $L_2$ . The output, then, becomes

$$\Delta V_o(dL_2) = \left\{ \frac{-2\omega^2 L_2^o (R_0^2 + R_0 R_2) + j \left( R_0 \omega^3 L_2^o{}^2 - R_0^3 \omega - 2R_0^2 R_2 \omega - R_0 R_2^2 \omega \right)}{\left[ (R_0 + R_2)^2 + (\omega L_2^o)^2 \right]^2} \right\} dL_2 \quad (4.55)$$

Now, the signals given by equations (4.53) and (4.55) are orthogonal since it can be shown that

$$\frac{f(dR_2)}{f(dL_2)} = \text{pure imaginary } j \text{ term} \quad (4.56)$$

Now, the length of the orthogonal trajectory,

$$|\Delta X_{L_2}| = \omega |\Delta L_2| \quad (4.57)$$

is related to  $|\Delta R_2|$  by the same calibration factor since, from (4.53) and (4.55),

$$\left| \frac{\omega f(dR_2)}{f(dL_2)} \right| = 1. \quad (4.58)$$

Theoretically, therefore, the resistors can completely calibrate an instrument. Chapter 5 uses these findings to experimentally calibrate two different eddy current instruments, and presents a method for converting a signal to a quantitative impedance measurement in ohms.

## CHAPTER 5. CALIBRATION

### 5.1. Introduction

The bridge circuit principle is often associated with the common eddy current measurement system. Circuit analysis has shown that a commercial eddy current instrument can be fully calibrated by inserting resistors in series with a test coil placed over a type of material that will be tested in the future. This simple, but effective method yields a calibration factor that directly relates the instrument's voltage change to an impedance change at each frequency. Throughout the process, the resistors are assumed to be pure real so that the impedance plane's real axis can be located, thereby reducing any measured impedance change to its real and imaginary components.

The calibration procedure, and the subsequent quantitative flaw measurement method, will be presented in a general manner that can be applied to most eddy current instruments. Calibration curves, and therefore calibration factors, were found for three probes each combined with two instruments; however, only those results for coil ISU 2 with both instruments A and B will be reported in this chapter because the procedure and results for the other probes are qualitatively similar. Finally, some very important instrument characteristics and observations will be discussed. These will include some interesting sensitivity features that were discovered during the calibration of instrument A with both probe ISU 2 and the ferrite probe ISU 5. As shown in Table 3.1, these two probes are dimensionally similar, but their inductances differ in accordance with their respective air and ferrite core.

## 5.2. Methods

### 5.2.1. Calibration procedure

The set up of Figure 3.1 is used to calibrate the instruments, which includes the calibration box of Figure 3.2. The calibration was done from 2 to 40 kHz in steps of 2 kHz, and 40 to 80 kHz in steps of 10 kHz by sequentially switching in the six resistors from 0.08 to 1  $\Omega$ ; this generated output signals, as shown in Figure 5.1, at each frequency. The measured voltages were stored in computer files in terms of the instrument's output signals,  $V_H$  and  $V_V$ . At least five separate measurements were performed so that a straight line fit could be obtained by linear regression from a plot of  $V_H$  vs.  $V_V$ . As shown in Figure 5.1, the direction of these signals defines the  $Z_{\text{real}}$  axis at one frequency, and its location is found in terms of the angle,  $\phi$ , from the horizontal  $V_H$  axis. The sign convention is given in Figure 5.1. It is important to maintain the same phase angle setting on the instrument to ensure the impedance plane's angular location will be constant on the instrument's screen during calibration as well as for all future flaw measurements.

The calibration for both instruments was performed with the probe placed over two 40 mil 2024 alloy plates, that were to be tested later for corrosion, on an area without corrosion or flaws. However, this was also done with the probe over an area with appreciable thinning (40%) in the top layer; there was no obvious difference in these two responses, other than what might be expected from random and experimental errors in the output voltage measurements. Thus, the assumption that the calibration factor is constant for the probe located on a 2024-T3 aluminum skin lap splice with and without

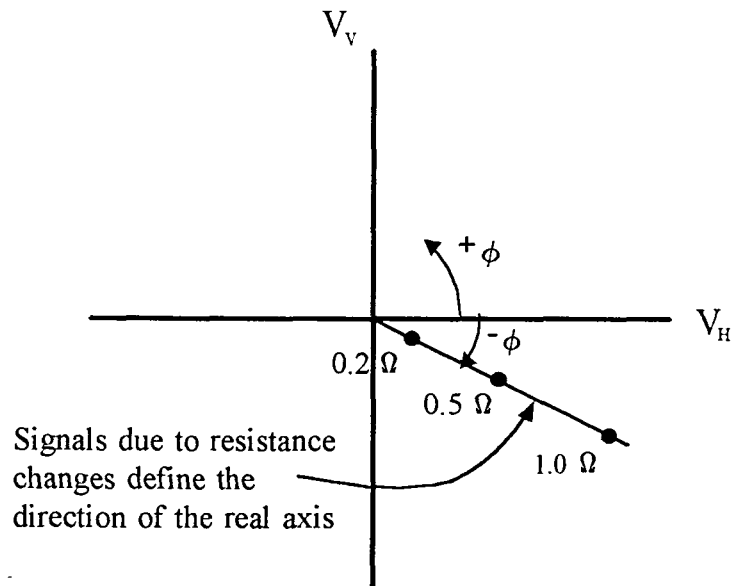


Figure 5.1: Output signals from resistors sequentially inserted between the coil and the instrument defining the real  $Z_{\text{real}}$  axis

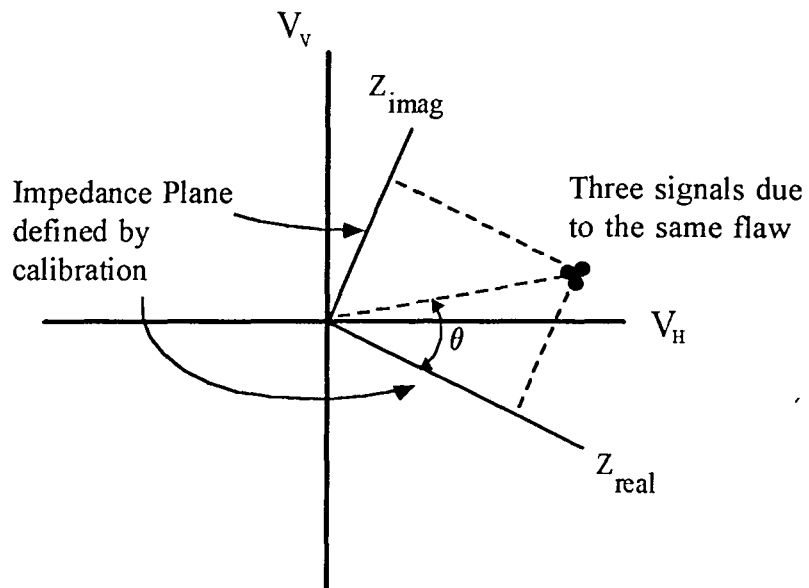


Figure 5.2: Flaw signals projected onto the calibrated impedance plane to determine flaw impedance quantitatively

corrosion is valid. Note that each instrument must be set at a constant gain setting throughout the calibration procedure, and its setting recorded for future reference when performing actual measurements.

5.2.1.1. Measuring the calibration resistors The resistors in the box shown in Figure 3.2 are nominal values; the actual values vary with frequency and had to be measured accurately with the impedance analyzer. This was done by subtracting a zero reading, the total complex impedance without a resistor switched into the circuit, from the total value when a resistor was switched into the circuit. Five separate swept frequency measurements were captured on a PC, yielding data files for each resistor with standard deviations. The results gave resistance change values for each resistor, as well as very small inductive reactance changes, at each frequency. The first two resistors of 0.01 and 0.04  $\Omega$  were found to have such small resistances that their inductances could not be ignored; hence, they were not used. The remaining resistors were assumed to have only pure real impedance since their inductive reactances were generally negligible at these relatively low frequencies. Thus, for the purpose of these calibration procedures, the total resistance changes were taken to be approximately equal to the total impedance changes, or  $\Delta Z \approx \Delta R$ , for resistors 0.08 to 1.0  $\Omega$  only.

The voltage magnitudes produced by the resistors were plotted vs. their total impedance changes to obtain calibration curves. As will be seen, these plots are linear relationships. Thus, the slopes of the resulting straight line fits can represent a calibration factor at each frequency, in V/ $\Omega$ .

### 5.2.2. Quantitative flaw measurements

We can graphically explain how quantitative measurements are made using the calibration curves. Figure 5.2 shows the position of the impedance plane defined by the calibration process. A relative signal due to any type of flaw, or material characteristic change, can be projected onto the real and imaginary axes to give the equivalent changes in terms of quantitative resistances and inductive reactances.

In practice, the total impedance magnitude is found in ohms by multiplying the total voltage output magnitude,  $\Delta V_o$ , by the inverse of the calibration factor and adding the intercept, if one exists. The resistive component, for example, would then be found by simply multiplying the result by the cosine of the angle,  $\theta$ , between the flaw signal and the real axis.

### 5.3. Calibration Curves for Instrument A

All curves shown herein are the results found with coil ISU 2. Figure 5.3 shows the voltage response for instrument A due to the resistors. This instrument exhibits an unusual amount of scatter at 18 kHz. But, typically, the responses are quite linear. Figure 5.4 gives the calibration curves; the calibration factors are determined from the slope of each line at each frequency. Notice the slopes decrease with increasing frequency. This observation is an important finding that will be discussed in a later section.

Linear regression yielded the straight line fits, given in Figure 5.4, each consisting of both a slope and an intercept. By statistical analysis [23], a 95% confidence interval was found for each line; however, only two are shown here as dotted lines, one of which contains the worst scatter at 18 kHz. Note that

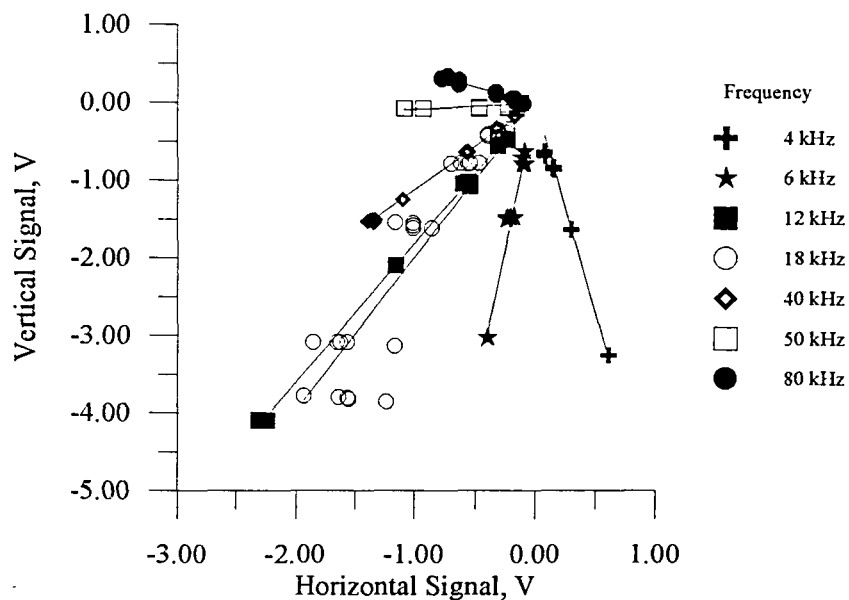


Figure 5.3: Vertical vs. horizontal voltage signal due to changing calibration resistors for instrument A at 30 dB gain

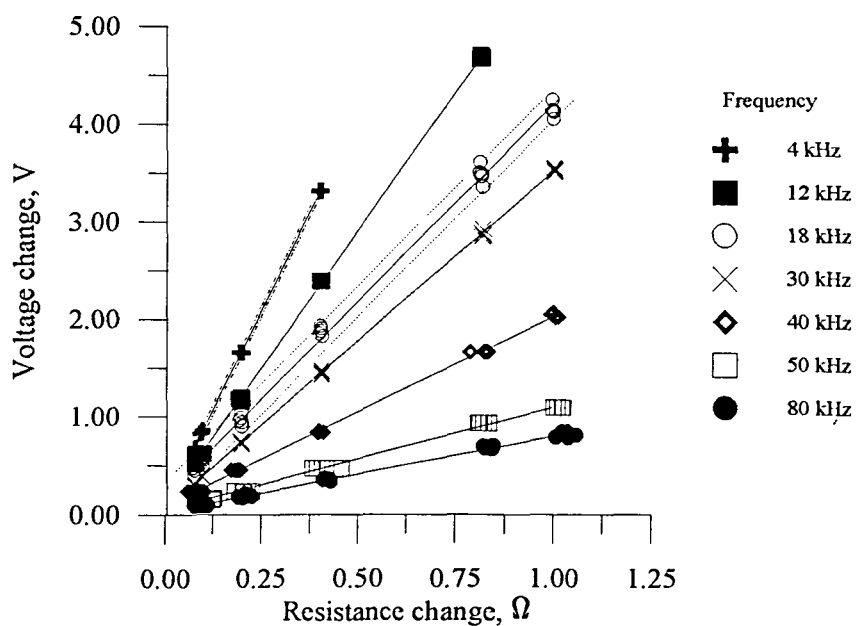


Figure 5.4: Magnitudes of signal voltage vs. resistance change for instrument A; slope equals the calibration factor

these graphs were not physically used to convert flaw signals to impedance changes. Rather, a computer program was written to perform the actual conversions, using the curves' straight line equations. The propagation of errors in the data as well as from the calibration curves' confidence intervals is accounted for during this conversion process using the error propagation formulae and statistical analysis given in [24].

#### **5.4. Calibration Curves for Instrument B**

The plots in Figures 5.5 and 5.6 are similar to those for instrument A. However, the linear responses have much less scatter than that exhibited by instrument A. The slopes shown in Figure 5.6 also represent the calibration factors, and they decrease with increasing frequency, as observed before.

#### **5.5. Important Observations**

Since the calibration factor is the output voltage response to a  $1 \Omega$  change in the test coil, this can be considered a measure of the instrument's sensitivity. As shown in Figure 5.7, the sensitivity of instrument A decreases with increasing frequency, and eventually flattens out, or saturates. This important behaviour is an inherent characteristic of this instrument. Furthermore, the sensitivity is a function of total probe impedance, as illustrated by the steeper curve for the higher impedance ferrite probe. The two probes, ISU 2 and ISU 5, are identical in size and number of turns, so that the effects of the ferrite alone could be examined.

These behaviors are explained by the circuit analysis performed in chapter 4. From equation (4.53), the calibration factor will decrease with

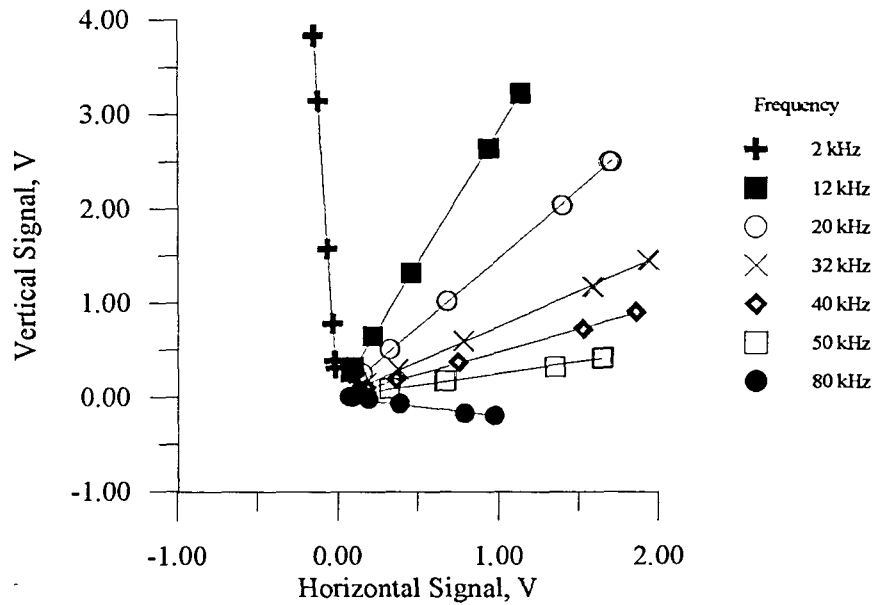


Figure 5.5: Vertical vs. horizontal voltage signal due to changing calibration resistors for instrument B at 63 dB gain

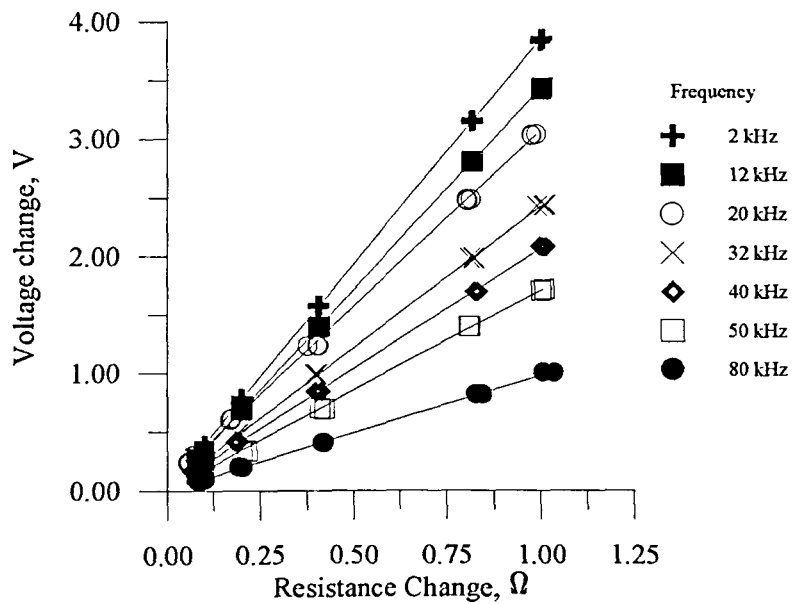


Figure 5.6: Magnitudes of signal voltage vs. resistance change for instrument B; slope equals the calibration factor

increasing frequency. Furthermore, a higher impedance probe will have a smaller calibration factor than a lower impedance probe. The ferrite in ISU 5 increases the inductance, hence the impedance, of the coil; this subsequently reduces the sensitivity of the instrument faster with frequency than with the similar, but lower inductance, air-core probe. These results show that the calibration curves, hence the calibration factors, are valid only for that particular probe-instrument combination used during the calibration procedure. Thus, the whole calibration procedure must be repeated when a different probe is used with that same instrument.

Figure 5.8 gives a comparison between the sensitivity of instrument A and B. Since these curves are based on data obtained at different gains, they should not be used for absolute or quantitative comparisons. However, they are useful to compare the instruments' overall performances. Given their respective gain settings of 30 dB and 63 dB, instrument A shows more sensitivity than instrument B at low frequencies, but then drops off quicker and saturates sooner. It is clear that the frequency response is different from one instrument to another, since this depends on the internal workings of the individual instruments.

It is important to note that characterizing flaws based on the interpretation of an uncalibrated signal's frequency response alone may be incorrect, since the instrument itself has a variable frequency response. However, the preceding calibration procedure allows an output to be measured in ohms. Hence, this compensates for the instrument's frequency response because that response is built into the calibration curves that are used to convert the measured signals into the coil's impedance change.

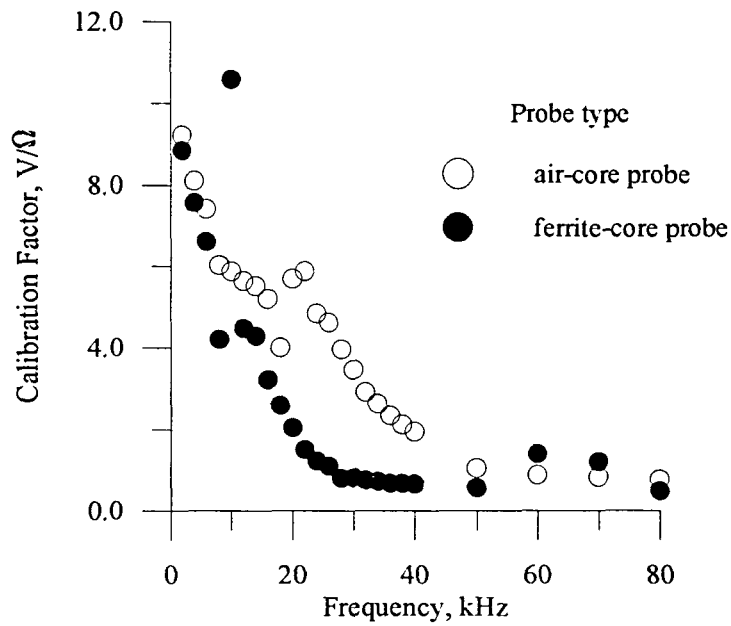


Figure 5.7: Effects of frequency and probe inductance on calibration factor, using coils ISU 2 and ISU 5

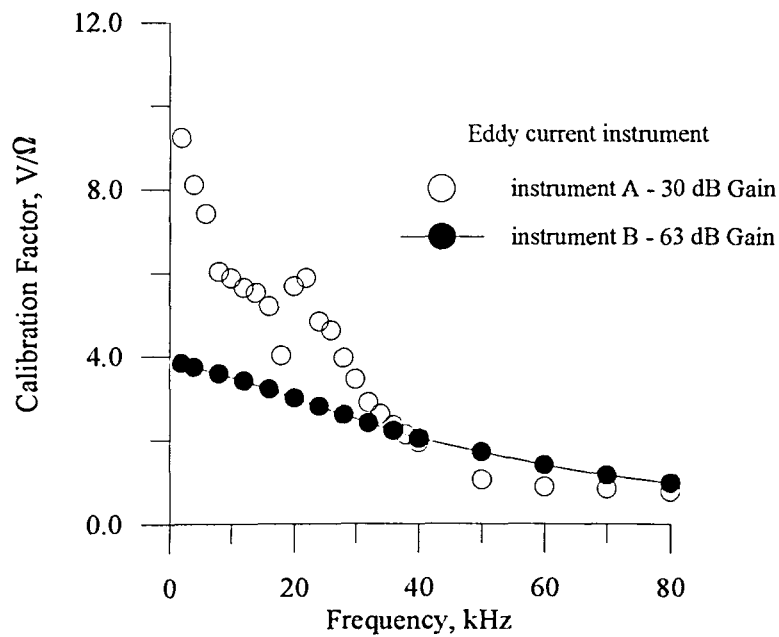


Figure 5.8: Comparison of calibration factor vs. frequency between instrument A and B

Finally, this type of exercise can also disclose certain performance characteristics of an instrument. Instrument A's curve in Figure 5.8 exhibits a scattered and discontinuous response between 18 to 22 kHz. This kind of information can be important to an operator when taking flaw measurements across these frequencies.

## CHAPTER 6. QUANTITATIVE ANALYSIS OF THINNED ALUMINUM LAP SPLICES

### 6.1. Introduction

Thinned aluminum alloy lap splices are quantitatively analyzed in this chapter using both the eddy current instruments and the 4194A HP impedance analyzer. First, swept frequency measurements of the machined samples will be compared to the forward theoretical solution using two air core-coils and the impedance analyzer. Also, specific features in the resistance change vs. frequency curve will be closely examined with respect to changes in the location of the thinned regions, the amount of thinning, and plate separation. Next, the calibrated eddy current instrument measurements will be compared to theory as well as to the impedance analyzer to illustrate the effectiveness of the calibration methods previously derived and the ability to adapt this technique to commercial instruments.

Subsequent inversions performed on the data from the impedance analyzer and instrument A for the machined samples described in section 3.4.1 will then be outlined. The inferred metal-air-metal layer thicknesses will be compared to the actual thicknesses to evaluate the method's accuracy. Inversion results for three artificially corroded samples will also be presented to evaluate the procedure for more realistic situations, again comparing them to the actual thinning amounts. Finally, the effects of ferrite core probes on the signal in comparison to the air core probes will be briefly studied.

## **6.2. Swept Frequency Impedance Measurements Of Machined Samples Using Air-core Eddy Current Probes**

Measurements on machined samples make up the majority of the eddy current evaluations because of the samples' known geometries. Each has been precisely measured with a micrometer to allow them to be modeled confidently by the theory previously described. The specimens consist of those plate samples given in Table 3.2 and oriented as shown in Figure 3.7. The two air core probes are specifically used here to allow theoretical predictions to be compared directly to experimental measurements. Most of the data presented herein are from measurements taken with coil ISU 2 described in chapter 3. However, some results for ISU 3, the larger diameter probe, are given for comparison and to further evaluate the theory's validity.

### **6.2.1. Impedance analyzer measurements and results**

6.2.1.1. Procedure The setup for measuring a test coil's impedance change has been described in chapter 3. When measuring thinned lap splices, the coil must first be placed onto a reference area of the sample that is completely free of defects or layer separation to obtain the "off" or "defect-free" measurement,  $Z'$ . Another impedance measurement is then taken with the coil positioned over the area with the machined flat-bottomed hole, labeled  $Z$ . In order to best represent the response of the flaws, each separate sample configuration was measured five times to obtain a mean and minimize random errors such as might arise from a tilted or a poorly secured probe. The averaging process yielded a sample standard deviation at each frequency point to represent the error bars on the impedance change vs. frequency graphs. All

swept frequency measurements were performed from 100 Hz to 100 kHz in 2 kHz steps. Both the real and imaginary components of the impedance change,  $\Delta Z = Z' - Z$ , as a function of frequency were captured by computer in a text file. However, only the resistive change,  $\Delta R$ , vs. frequency plots are presented in the following results.

#### 6.2.1.2. Results with coil ISU 2: experimental data vs. theory

Measurements and calculations of  $\Delta R$  vs. frequency curves for coil ISU 2 are given in Figure 6.1 to 6.4 for the four different thinned regions. Three representative thinning amounts, ranging from about 10% to 30% thinning, are shown in each figure. In general, the experimental data show good agreement with the theoretical curves.

#### 6.2.1.3. Discussion

As discussed in chapter 4, these curves each have features that depend on the both the amount and the location of the thinned region. The frequency at which the minimum,  $\Delta R_{\min}$ , occurs clearly shifts to lower frequencies as the corrosion's location moves down from the top layer, as in Figure 6.1, to the bottom surface, as in Figure 6.4. This is illustrated more clearly in Figure 4.8. This observation illustrates the reason a frequency sweep can be used to determine where the corrosion has occurred in a specimen. A significant frequency shift also occurs when the amount of metal loss varies in the top layer, as shown in Figure 6.1. This is not as evident in the other three cases. This effect may be related to the metal-air gap interface's position with increasing metal loss. Thinning in the top layer is the only location where the interface moves as the amount of thinning is changed. Thus, as the thinning increases, the interface moves up towards the

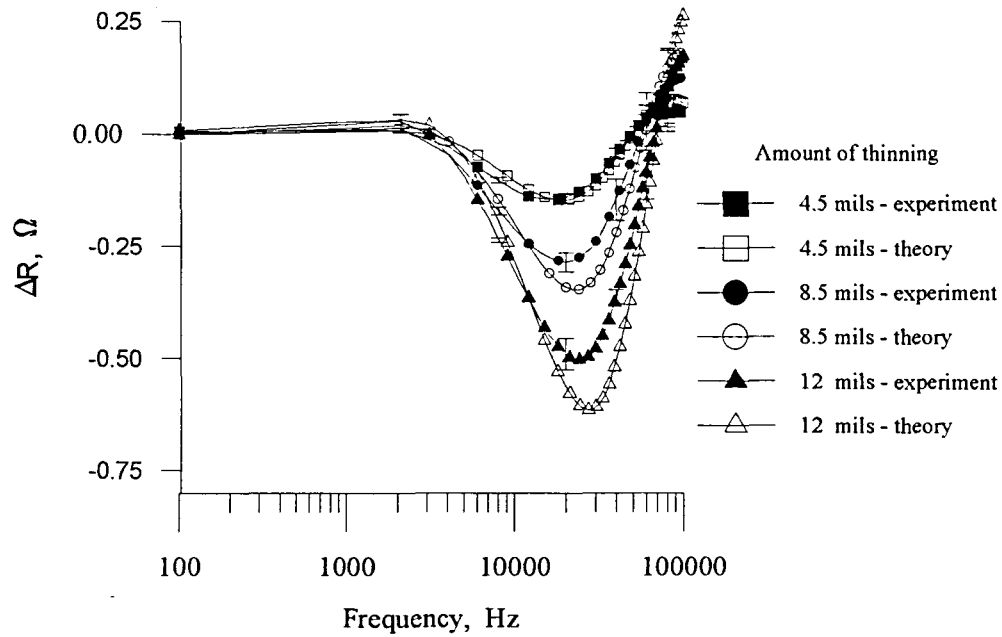


Figure 6.1: Coil ISU 2; experimental and theoretical resistance change vs. frequency for various amounts of thinning in the first layer

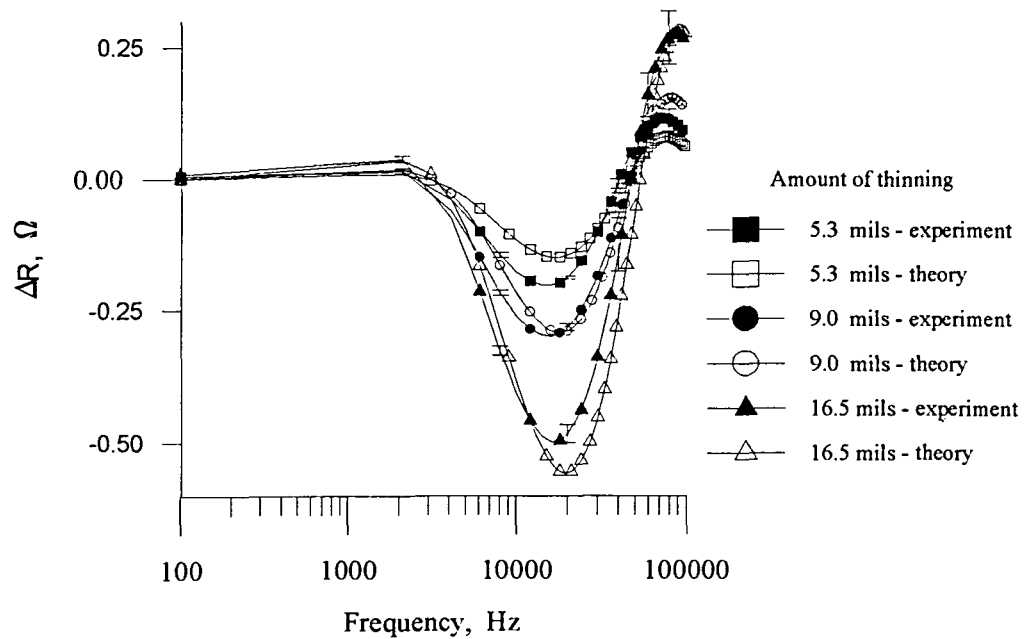


Figure 6.2: Coil ISU 2; experimental and theoretical resistance change vs. frequency for various amounts of thinning in both layers

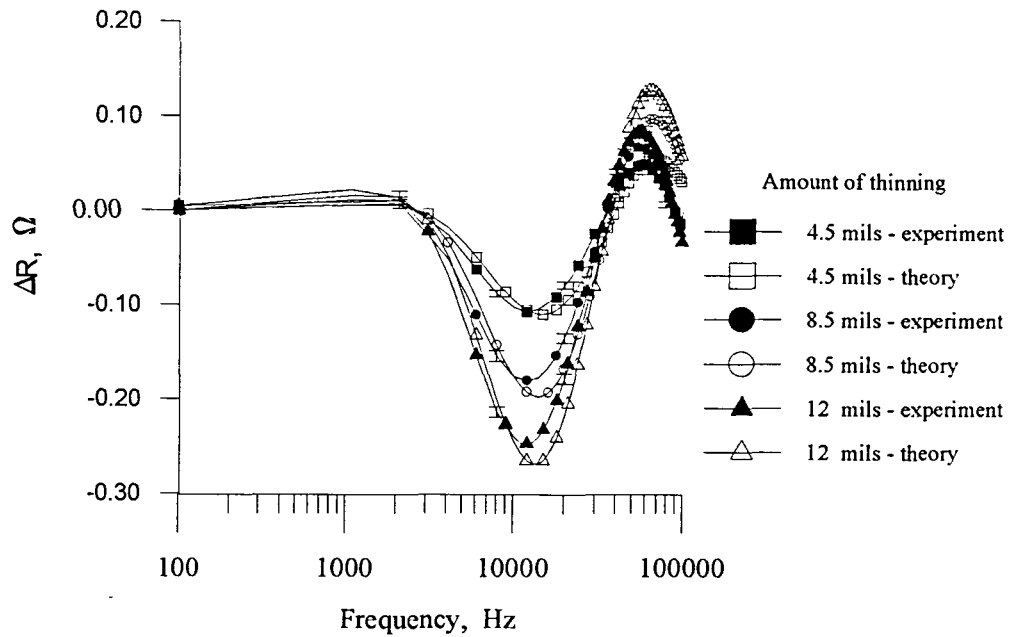


Figure 6.3: Coil ISU 2; experimental and theoretical resistance change vs. frequency for various amounts of thinning in the second layer

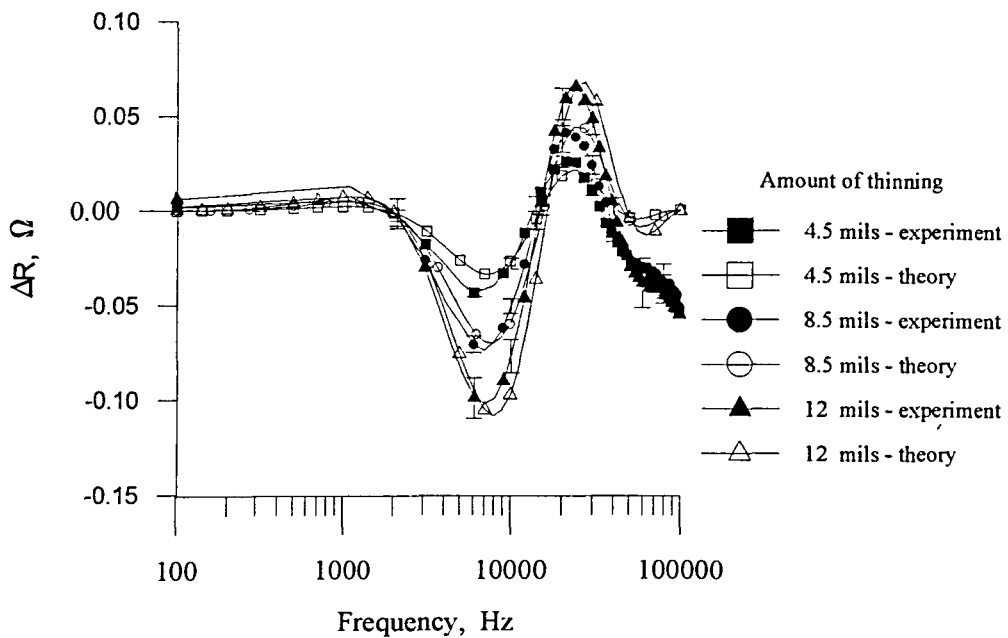


Figure 6.4: Coil ISU 2; experimental and theoretical resistance change vs. frequency for various amounts of thinning on the bottom surface

coil, so the higher frequencies will see more changes in  $\Delta R$ , due to the skin effect.

Any small discrepancies between the theory and the experimental can be attributed to several factors. First, the theory is based on several assumptions, such as uniform windings and uniform layer thicknesses. Hence, an imprecisely wound coil, resulting in an imperfect wire packing, will cause some errors in the model. Actual physical variances between the model and the actual parameters of coil will also affect the agreement. The model cannot account for built-in tilt in the test coil. An informal performance test of the two air-core coils, based on the photoinductive field-mapping procedure of Moulder and Nakagawa [25], revealed that both these coils exhibit a significant amount of tilt. The curves of Figure 6.1 and 6.2 seem to be affected by these imperfect modeling factors more than the others.

In addition, the machined holes are not perfectly uniform, as indicated in section 3.4, nor are the sample plates perfectly flat in the holding apparatus. The exact probe position and air gaps due to warping of the aluminum plates can therefore affect the magnitude of  $\Delta R_{\min}$  and the resulting experimental curves.

6.2.1.4. Results with coil ISU 3: experimental data vs. theory The coil ISU 3, having a larger diameter, was used for fewer, but similar eddy current measurements to those made with ISU 2. In the process, however, the resulting swept frequency curves were unexpectedly found to disagree with theory, using the initial design lift-off of 0.25 mm (same as for coil ISU 2) as an input parameter. However, what is believed to be a representative lift-off value was found by adjusting the value of this parameter in the theoretical

model until most curves agreed with the experimental ones. The resulting lift-off was 0.45 mm, as given in Table 3.1. The results for two locations, first layer and second layer thinning, are reported here in Figures 6.5 and 6.6. With the corrected lift-off, the agreement is good and comparable to that of coil ISU 2.

Note that all the coils were designed to have the same lift-off of 0.25 mm. The inaccurate lift-off in coil ISU 3 was probably caused by an error made during its manufacture.

6.2.1.5. Effects of layer separation Impedance analyzer data, with coil ISU 2, were compared to theory for the case where only plate separation exists, and also when it is combined with thinning in the first or second layer. The separation was simulated with thin plastic sheets, 4 mils thick, placed between the two aluminum plates. As shown in Figure 6.7, the results show good agreement with theory when separation occurs with no thinning. The separation affects the swept frequency curve as shown in Figure 6.8, which compares it to a curve for an equivalent amount of thinning without separation. The location of the minimum is close to that of the first layer thinning; however, their magnitude and first zero crossings are different. The second layer thinning differs noticeably from separation because of the characteristic frequency shift. These feature differentiations should, therefore, allow one to discriminate between plate separation and actual thinning. Note that, as expected, the superposition of these two curves results in the response found for combined second layer thinning and separation.

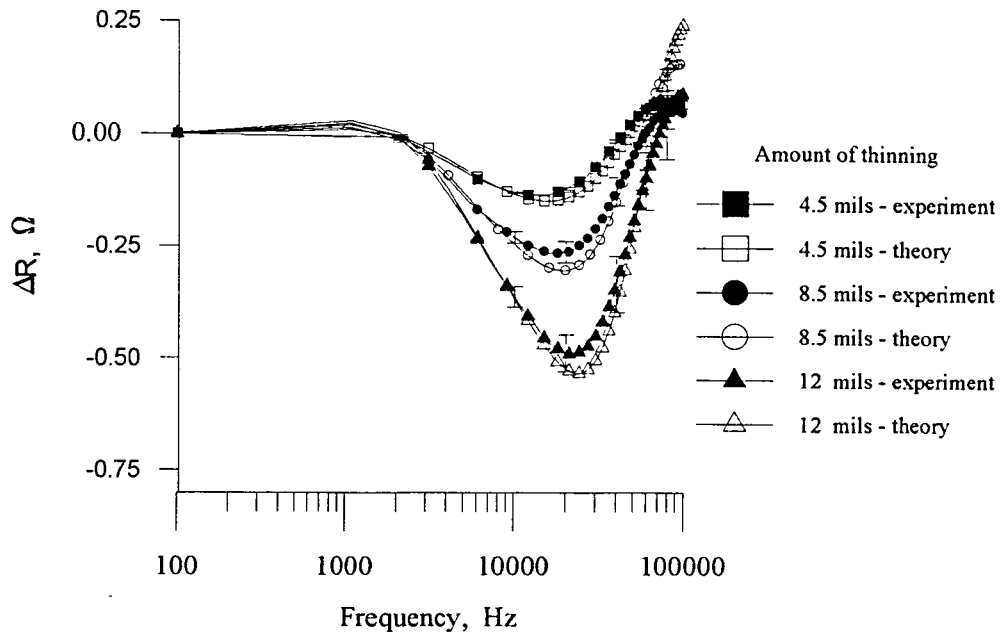


Figure 6.5: Coil ISU 3; experimental and theoretical resistance change vs. frequency for various amounts of thinning in first layer

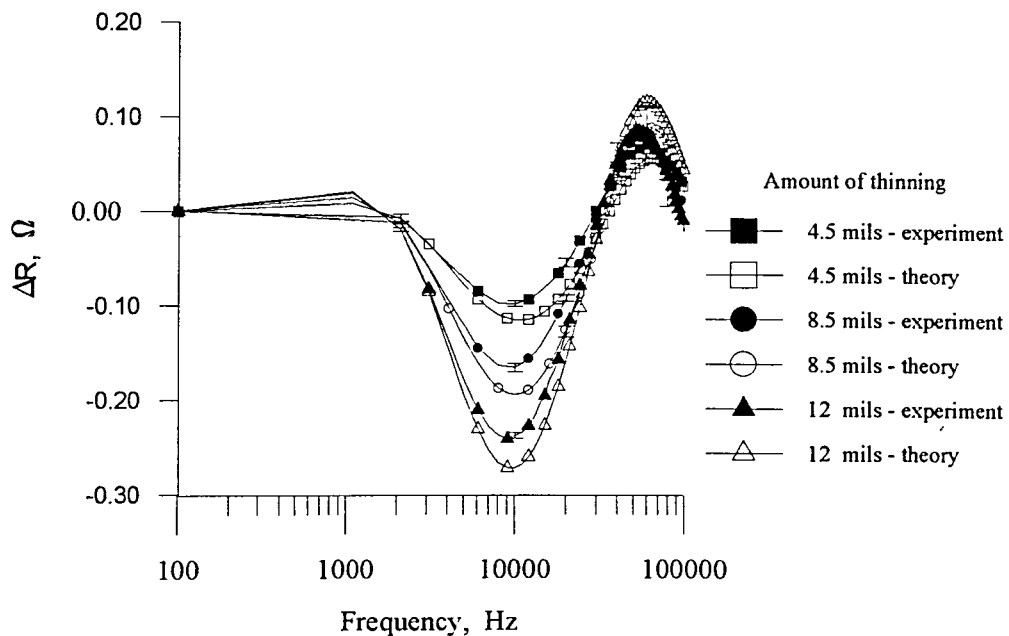


Figure 6.6: Coil ISU 3 experimental and theoretical resistance change vs. frequency for various amounts of thinning in second layer

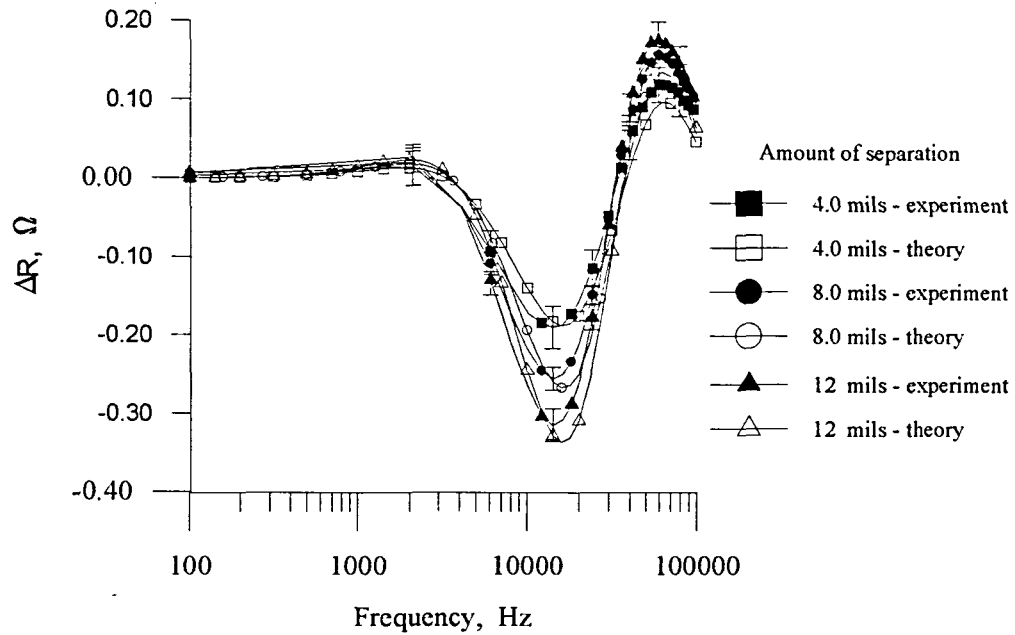


Figure 6.7: Experimental and theoretical resistance change vs. frequency for various amounts of separation between layers, all with 4.5 mils thinning in second layer; impedance analyzer

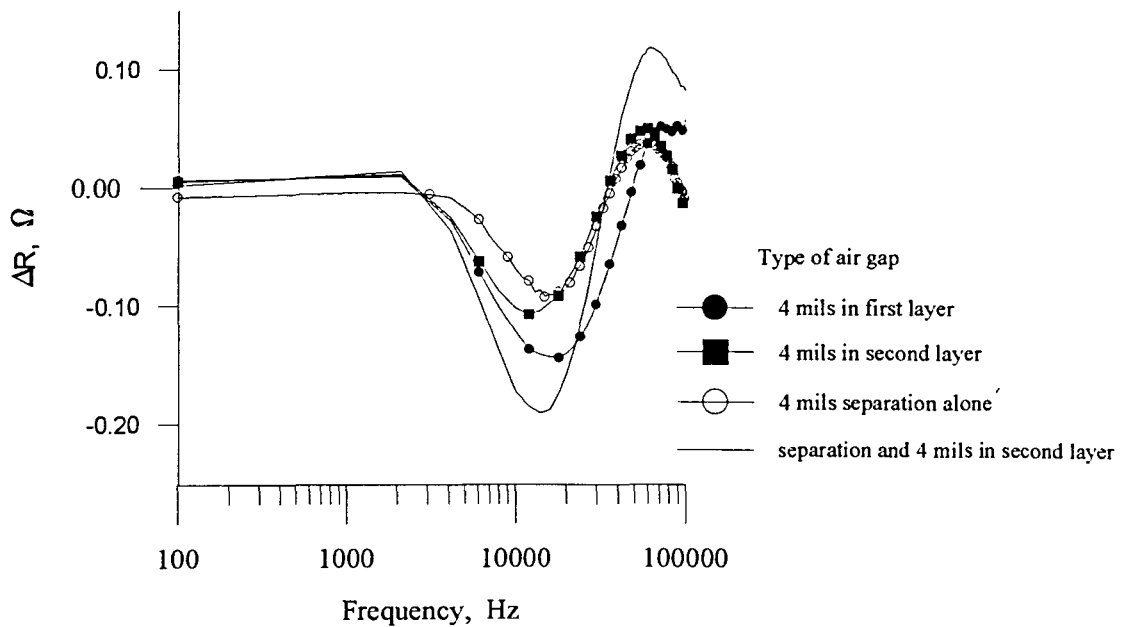


Figure 6.8: Comparison between separation alone, thinning alone, and second layer thinning with separation; impedance analyzer

### 6.2.2. Instrument A measurements and results

The procedure here is very similar to that used with the impedance analyzer, except that each  $Z'$  and  $Z$  measurement must be done in steps for every four frequencies, since it can measure only four frequencies at once. As indicated in chapter 3, the eddy current instrument is nulled for the probe's  $Z'$  position between each  $Z$  measurement. An instrument gain setting is chosen in each case to produce a measurable signal without over amplifying the electronic noise. The data is stored in a computer as horizontal and vertical voltages, then converted to resistive changes using the calibration factors and quantitative flaw measurement methods of chapter 5.

A few representative results in Figure 6.9 and 6.10 are given to show that this instrument agrees well with both the impedance analyzer and theory. As expected, scatter is more pronounced with instrument A because the extra steps involved in the calibration and conversion process add more sources of error, hence more noise. The large amount of scatter between 18-22 kHz is mostly due to the inaccuracy of the calibration curves at these frequencies, especially for small impedance changes. The noise from this source propagates to the swept frequency curves from the impedance conversion process.

### 6.2.3. Instrument B measurements and results

The procedure is a duplicate of the one for instrument A, except that only one frequency can be measured at a time. Obviously, this significantly increases the time for each swept frequency measurement. Only two sets of measurements were completed with instrument B simply to demonstrate that

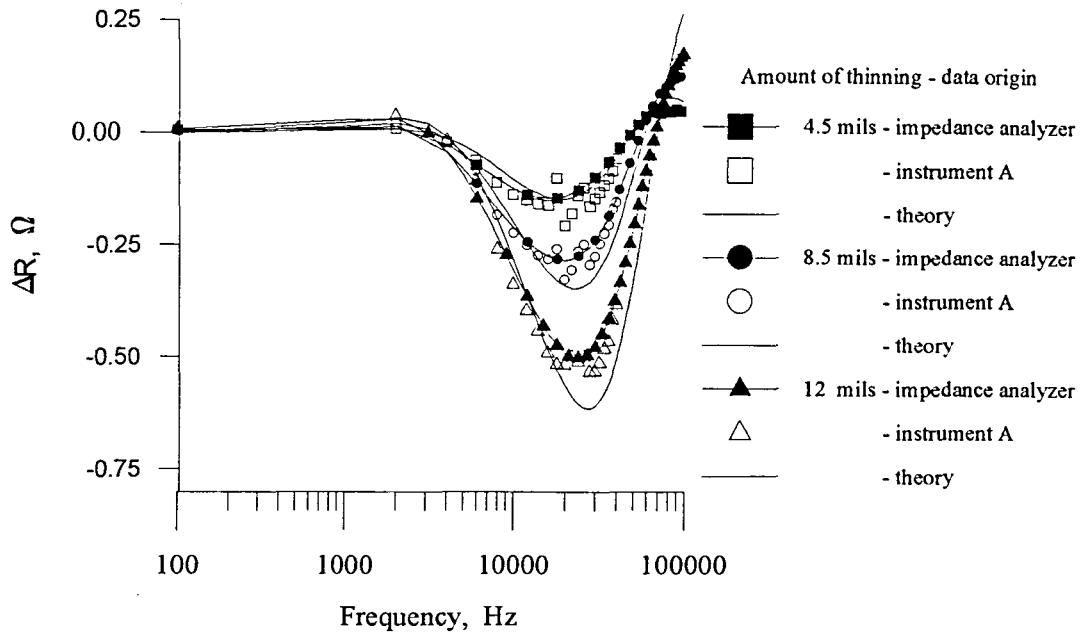


Figure 6.9: Comparison between impedance analyzer, instrument A, and theory for first layer thinning

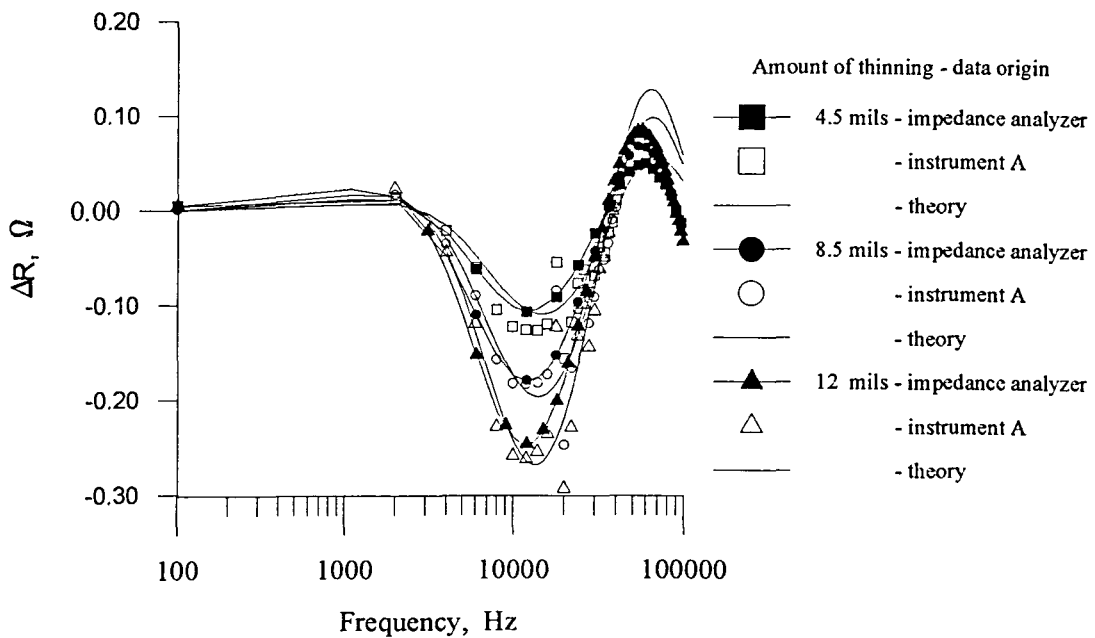


Figure 6.10: Comparison between impedance analyzer, instrument A, and theory for second layer thinning

this eddy current method can work with a different instrument and, most likely, with almost any other commercial instrument as well. Figure 6.11 confirms this by illustrating the good agreement obtained when this instrument's measurements are compared with both theory and the impedance analyzer. Only the forward problem was analyzed with this instrument.

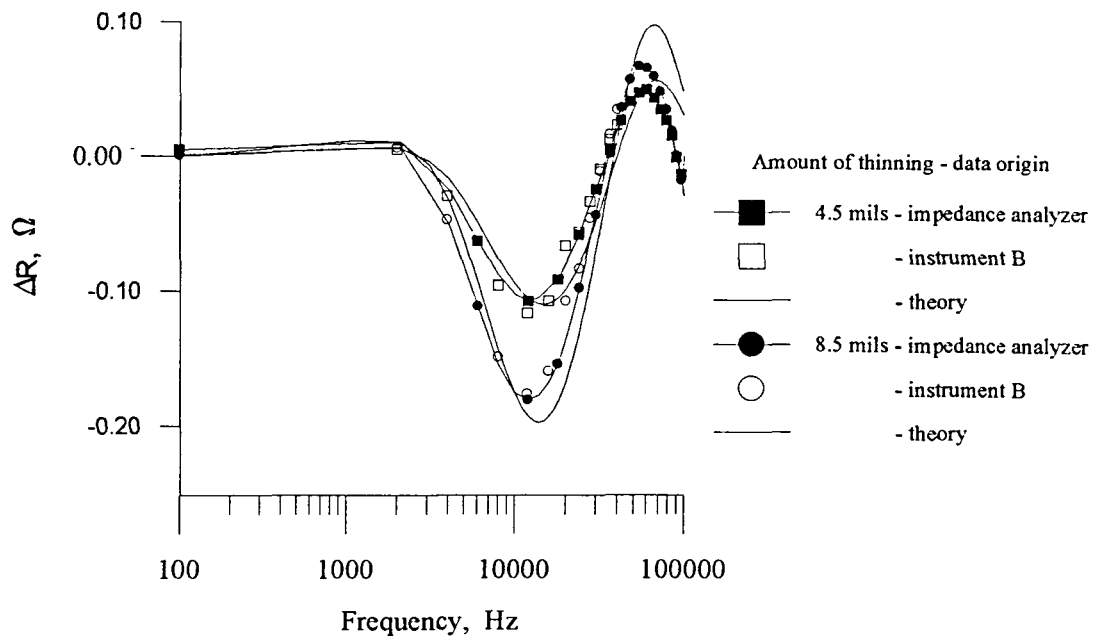


Figure 6.11: Comparison between impedance analyzer, instrument B, and theory for second layer thinning

#### 6.2.4. Inversion of experimental data

6.2.4.1. Procedure Experimental data from both the impedance analyzer and instrument A were inverted to determine the accuracy of the inferred layer thicknesses and hence test the effectiveness of this technique for quantitative corrosion characterization. The inversion method has already

been described in section 4.6. Twenty points from 2 to 40 kHz from each data set were used in all cases, limiting the minimization routine to that range of frequencies where the  $\Delta R$  curve has the most structure: between the zero crossings. Each inversion ran for 100 iterations. The inversions were only performed for those samples that simulate thinning (air gap) in one of the three regions between the plates, not for metal loss on the bottom of the second plate. However, as mentioned in section 4.6, the algorithm's nature allows the air gap's location to be determined by inferring the three metal-air-metal layer thicknesses without having to provide it with any initial location information. Note that no data from instrument A were discarded for these inversions, including the scattered points between 18 and 22 kHz shown in Figure 6.9.

6.2.4.2. Inversion results Tables 6.1 and 6.2 show some of the inversion results for the impedance analyzer's experimental data using coil ISU 2. These represent the best and worst inversions obtained with this instrument, respectively. Similarly, Tables 6.3 and 6.4 are the results for instrument A. All the remaining results, for both coils ISU 2 and ISU 3, are given in the tables found in appendix B. The inferred quantities are presented in terms of the three layers shown in Figure 4.3(a) of regions 4, 3 and 2, corresponding to the first metal layer, the air gap, and the second metal layer respectively. Note how the location of thinning is easily discerned by the three thicknesses. For example, in Table 6.1 the inferred layers each have a top (first) layer of about 40 mils, which is the original thickness of the uncorroded aluminum plate, suggesting the thinning is in the second layer. A more graphical perspective of these results is given in Figures 6.12 and 6.13,

Table 6.1. Inferred metal-air-metal layer thicknesses from impedance analyzer swept frequency measurements using coil ISU 2; machined samples thinned in the second layer

<u>Actual thicknesses (mils)</u>			<u>Inferred thicknesses(mils)</u>		
First layer	Air gap	Second layer	First layer	Air gap	Second layer
40.0	4.5	35.5	42.2	4.8	31.6
40.0	8.5	31.5	41.1	8.3	28.6
40.0	10.0	30.0	40.7	9.4	26.9
40.0	12.0	28.0	40.3	10.3	25.5
40.0	16.0	24.0	41.6	15.3	22.3

Table 6.2. Inferred metal-air-metal layer thicknesses from impedance analyzer swept frequency measurements using coil ISU 2; machined samples thinned in both layers

<u>Actual thicknesses (mils)</u>			<u>Inferred thicknesses(mils)</u>		
First layer	Air gap	Second layer	First layer	Air gap	Second layer
37.2	5.3	37.5	38.3	8.1	33.3
35.5	9.0	35.5	36.8	11.8	33.0
32.0	16.5	31.5	34.8	19.0	31.8

Table 6.3. Inferred metal-air-metal layer thicknesses from instrument A swept frequency measurements using coil ISU 2; machined samples thinned in the second layer

<u>Actual thicknesses (mils)</u>			<u>Inferred thicknesses(mils)</u>		
First layer	Air gap	Second layer	First layer	Air gap	Second layer
40.0	4.5	35.5	39.9	5.2	35.3
40.0	8.5	31.5	38.6	7.2	31.5
40.0	10.0	30.0	40.3	10.9	32.0
40.0	12.0	28.0	38.9	10.3	27.7
40.0	16.0	24.0	38.2	12.9	24.3

Table 6.4. Inferred metal-air-metal layer thicknesses from instrument A swept frequency measurements using coil ISU 2; machined samples thinned in both layers

<u>Actual thicknesses (mils)</u>			<u>Inferred thicknesses(mils)</u>		
First layer	Air gap	Second layer	First layer	Air gap	Second layer
37.2	5.3	37.5	36.5	8.9	34.5
35.5	9.0	35.5	35.7	11.3	40.6
32.0	16.5	31.5	33.0	18.5	33.3

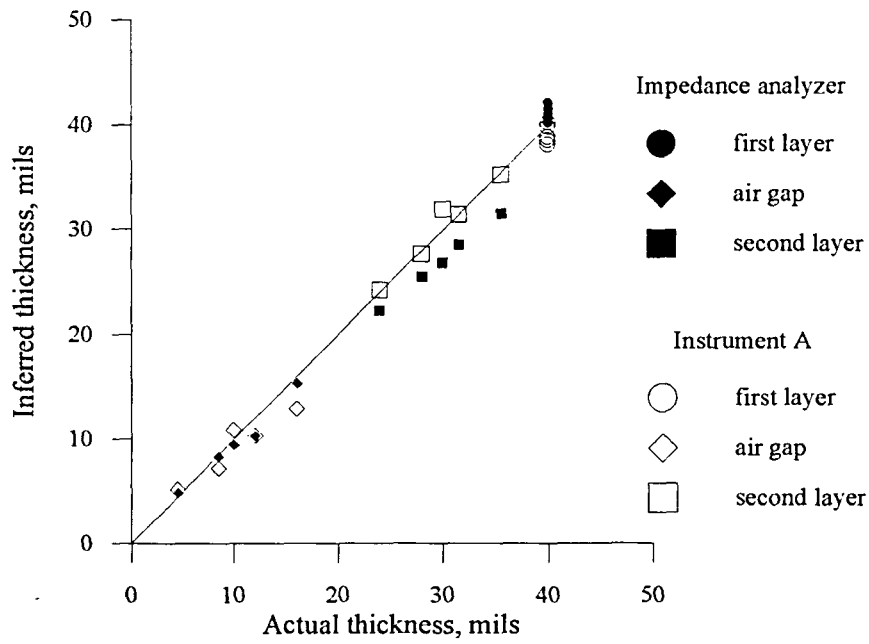


Figure 6.12: Actual layer thicknesses vs. those inferred from swept frequency measurements for machined samples thinned in the second layer

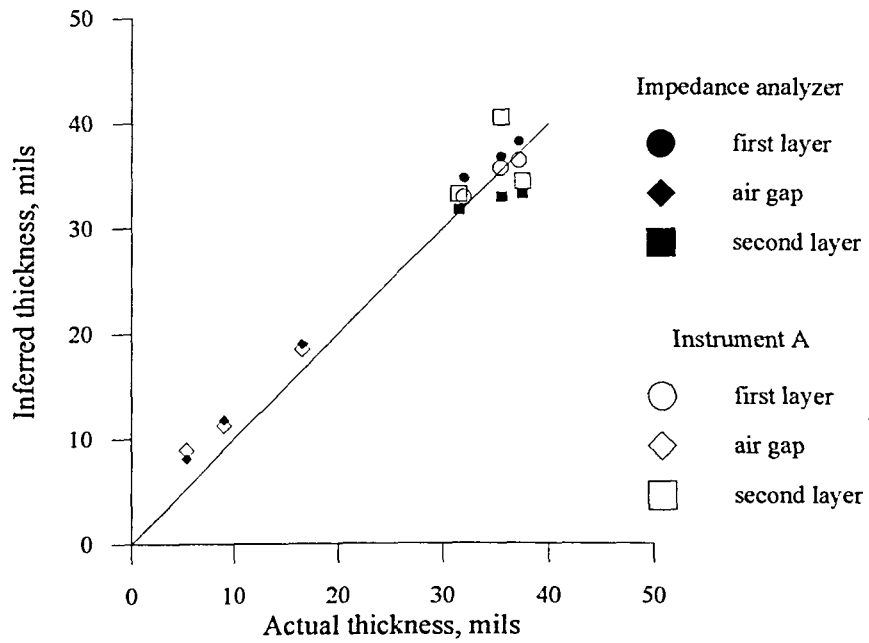


Figure 6.13: Actual layer thicknesses vs. those inferred from swept frequency measurements for machined samples thinned in both layers

as well as in appendix C for the tables in appendix B, where the actual vs. inferred quantities are plotted. These figures compare the inferred thicknesses to the actual thicknesses of the three metal-air-metal layers for both the impedance analyzer and instrument A on the same graph for easy comparison. Each graph represents one of the three different thinned regions measured with one of the two air-core coils.

6.2.4.3. Discussion Several initial observations are worth noting. First, the inversions generally infer the first layer thickness and the air gap more accurately than the second layer. All the graphed inversion results illustrate this inaccuracy clearly. This is expected since the signals related to deeper eddy current penetration, such as is required for second layer characterization, will tend to be weaker. For example, the standard depth of penetration, or skin depth, is less than 75 mils at frequencies above 4 kHz and less than 40 mils above 13 kHz. Since the second layer is located between 40 and 80 mils from the top surface, the current density is very low in that layer. Second, the inversions are the least accurate for the case where thinning occurs in both layers simultaneously. Third, coil ISU 3 gave better results than ISU 2 for all three inferred thicknesses and all locations. Note, however, that this conclusion is based on fewer measurements than coil ISU 2. Since these inversions can be sensitive to coil imperfections, it can be said that coil ISU 3 is a more precisely wound coil, or that its parameters are more accurately known, despite the lift-off problem encountered during the measurement process. But, its size may also be a factor. Since both coils ISU 2 and 3 have the same inductance, their field strengths should be similar; however, a larger diameter coil has a favorable impact on the sensitivity due

to a spatial effect that allows greater penetration into the material being tested [14].

Figures 6.12 and 6.13 are used to directly compare the effectiveness of instrument A to the impedance analyzer. The most unexpected outcome in these results is the surprising accuracy obtained from instrument A. However, the overall performance of both instruments are very good.

Errors in the inferred quantities compared to the actual values were found and tabulated for the four combinations of instrument and coil in Table 6.5. Note that these errors can be considered as a measure of sensitivity. For example, instrument A is sensitive enough to detect and measure the three layer thicknesses in a corroded lap splice with an mean accuracy of 1.3, 1.6 and 1.6 mils respectively. These were evaluated by averaging the errors in each of the three thicknesses inferred. The plus sign (+) signifies that the inversion always overestimated the actual thickness of that layer, the minus sign (-) underestimated them, and the plus or minus sign ( $\pm$ ) varied both ways. From these numbers, coil ISU 3 again shows greater

Table 6.5. Average accuracy of the four instrument/coil combinations in inferring layer thicknesses

Instrument/coil combination	First metal layer (mils)	Air gap layer (mils)	Second metal layer (mils)
4194A / ISU 2	+ 1.8	$\pm$ 1.1	- 2.4
4194A / ISU 3	+ 1.2	$\pm$ 0.7	$\pm$ 1.3
instr A / ISU 2	$\pm$ 1.3	$\pm$ 1.6	$\pm$ 1.6
instr A / ISU 3	$\pm$ 1.3	$\pm$ 0.7	$\pm$ 1.0

accuracy than ISU 2. Also, as discussed above, the sensitivity of the eddy current instrument A is very good.

Inversions were also performed on data from the plate separation experiments to determine if this method can differentiate between thinning due to corrosion and the separation of the layers not associated with corrosion, as expected from the forward measurements in section 6.2.1. Again, separation is not an input parameter in the inversion algorithm. This experiment was intended to test the algorithm's ability to infer the dimensions of lap splice specimens with separation without prior knowledge. A look at the results in Tables B.3 and B.4 reveals that the inversion overestimates thinning in the second layer by an average of 7 mils when in reality it is mostly, or all, separation, such as when the plates are warped or deformed. The first layer and total air gap, however, are reasonably accurate, with up to 2 and 1.2 mils error respectively.

### **6.3. Corrosion Sample Measurements**

#### **6.3.1. Procedure**

The measurement procedure was similar to both the impedance analyzer and instrument A methods for the machined hole samples. All the corrosion samples were measured with coil ISU 2. The probe was placed at the center of the corroded area shown in Figure 3.6(b) for measuring Z. The type-1 samples, 1b and 2b, were each measured separately with their respective uncorroded plates in the two orientations that simulate thinning in the first layer, then the second layer, as depicted in Figure 3.7(a) and (b), respectively.

The two corrosion samples were then positioned facing each other to simulate thinning in both layers, as in Figure 3.7(c). However, the two plates have different thicknesses, a case that hasn't been tested with the machined samples, with the 40 mil plate as the top layer and the 61 mil plate as the bottom layer in the lap splice.

Finally, the artificially corroded type-2 riveted lap splice sample was measured with both the impedance analyzer and instrument A. Note that the probe's lift-off had to be increased by 3 mils in the inversion procedure to compensate for the extra lift-off due to the paint.

### **6.3.2. Inversion results**

The inversion results for the type-1 samples are found in Tables 6.6 and 6.7. They are also shown graphically in Figure 6.14 and 6.15 for the impedance analyzer and instrument A respectively. The results and accuracies for the corroded samples were moderate to good; however, they are not quite as accurate as the inversions for the machined samples. Actual corroded sample thicknesses are more difficult to infer than machined samples because they usually do not exhibit completely uniform thinning, and the roughness due to the pitting may adversely affect the impedance measurements. It is interesting to note that the average accuracies shown in Table 6.8 indicate instrument A to be slightly more accurate in inferring the two metal layers than the impedance analyzer. This is surprising, especially since seven largely scattered and discontinuous swept frequency data points from instrument A were discarded from each data file, leaving only 13 points on the curve for the inversion process to search on. However, eddy current instruments are

Table 6.6. Inferred metal-air-metal layer thicknesses from impedance analyzer swept frequency measurements using coil ISU 2; corrosion samples thinned in first, second or both layers

<u>Actual thicknesses (mils)</u>			<u>Inferred thicknesses(mils)</u>		
First layer	Air gap	Second layer	First layer	Air gap	Second layer
35.2	4.8	40.0	37.4	5.3	36.6
40.0	4.8	35.2	40.7	5.3	35.2
56.5	4.5	61.0	50.5	3.3	66.8
61.0	4.5	56.5	63.4	6.4	54.9
35.2	9.3	56.5	36.3	8.9	59.8

Table 6.7. Inferred metal-air-metal layer thicknesses from instrument A swept frequency measurements using coil ISU 2; corrosion samples thinned in first, second or both layers

<u>Actual thicknesses (mils)</u>			<u>Inferred thicknesses(mils)</u>		
First layer	Air gap	Second layer	First layer	Air gap	Second layer
35.2	4.8	40.0	35.5	5.9	36.5
40.0	4.8	35.2	40.8	5.7	34.8
56.5	4.5	61.0	55.2	3.8	62.3
61.0	4.5	56.5	59.6	3.6	56.1
35.2	9.3	56.5	36.2	11.1	50.5

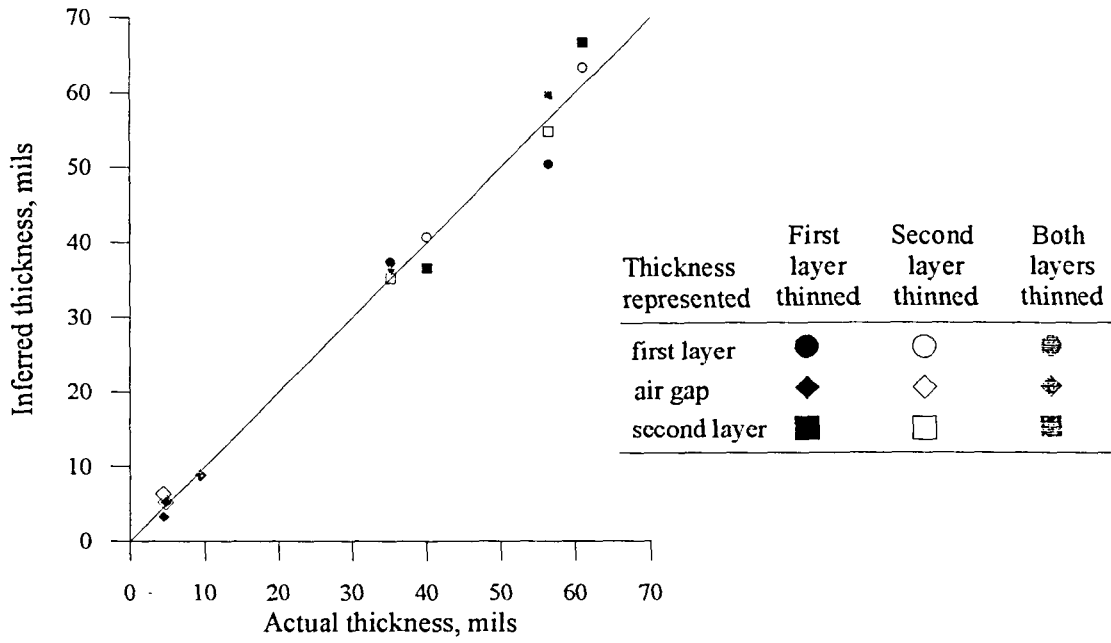


Figure 6.14: Corrosion samples' actual layer thicknesses vs. those inferred from the impedance analyzer swept frequency measurements

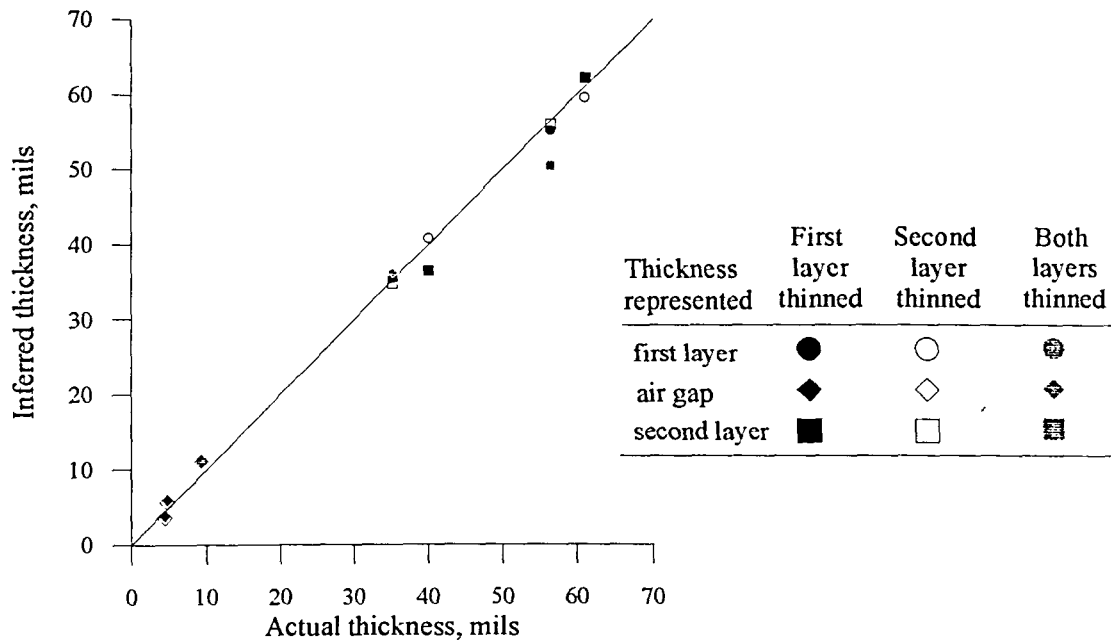


Figure 6.15: Corrosion samples' actual layer thicknesses vs. those inferred from instrument A swept frequency measurements

Table 6.8. Average accuracy in inferring layer thicknesses of corroded type-1 samples with coil ISU 2

Instrument	First metal layer (mils)	Air gap layer (mils)	Second metal layer (mils)
4194A	$\pm 2.5$	$\pm 0.9$	$\pm 2.9$
instr A	$\pm 1.0$	$\pm 1.1$	$\pm 2.3$

designed to be sensitive to very small coil impedance changes, allowing them to detect very small defects. Furthermore, we have seen in chapter 5 that instrument A is more sensitive at low frequencies, accounting for greater accuracy, especially for second layer corrosion.

The riveted type-2 sample's inferred thicknesses are 39.3, 19.3, and 38.8 mils, suggesting that the air gap is almost all separation, with 1.2 mils of metal loss in the second layer. The implied 17.4 mils of separation is significantly less than the estimated 22 mils. However, considering the large 7 mil error found in section 6.2.4 for second layer thinning in the presence of separation, such discrepancies in the separation samples can be expected.

#### 6.4. Experimental Measurements Using Ferrite-core Probes

##### 6.4.1. Comparison of ferrite-core to an air-core coil

The effects of adding a ferrite core to a coil were studied empirically by measuring the same machined samples for second layer and bottom surface thinning that were used to obtain the results in Figure 6.2 and 6.4 for the air-core probe ISU 2. Probe ISU 5 has a ferrite core; otherwise, it is nominally

identical to probe ISU 2, as given by Table 3.1. Since the theory covered in this thesis is limited to only air-core coils, no comparisons can be made in this respect. Although the accuracy of coil ISU 5's design parameters is not known, it is assumed that they are identical to ISU 2, notwithstanding the discrepancy discovered in coil ISU 3's lift-off. This enables a direct comparison between the two coils' swept frequency responses to be carried out to evaluate the ferrite's role. These comparisons are given in Figure 6.16 and 6.17 for the weak signals produced from second layer and bottom surface thinning. The first obvious effect of the ferrite is to increase the amplitude of the minimum by a factor of about 2.9 to 3.3, depending on the curve in question. However, a closer examination of the increase in  $\Delta R$  strength along the whole length of a particular pair of curves reveals that this ratio, or "strength factor", consistently decreases with increasing frequency.

#### 6.4.2. Discussion

The ferrite's primary purpose is to strengthen the signal amplitudes with its larger inductance and magnetic field strength. This makes a probe more sensitive to smaller flaws or thinning amounts. In this case, it especially improves the 4.5 mil bottom surface thinning response in Figure 6.17 from a resistance change of less than  $0.05 \Omega$  to about  $0.15 \Omega$ . This increases the signal to noise ratio for more accurate analysis. However, the main disadvantage of the ferrite-core probe is that it cannot be modeled analytically, and one must resort to numerical methods.

One way to adapt these quantitative eddy current techniques to ferrite-core coils would be to empirically characterize the probe's signal strength, for

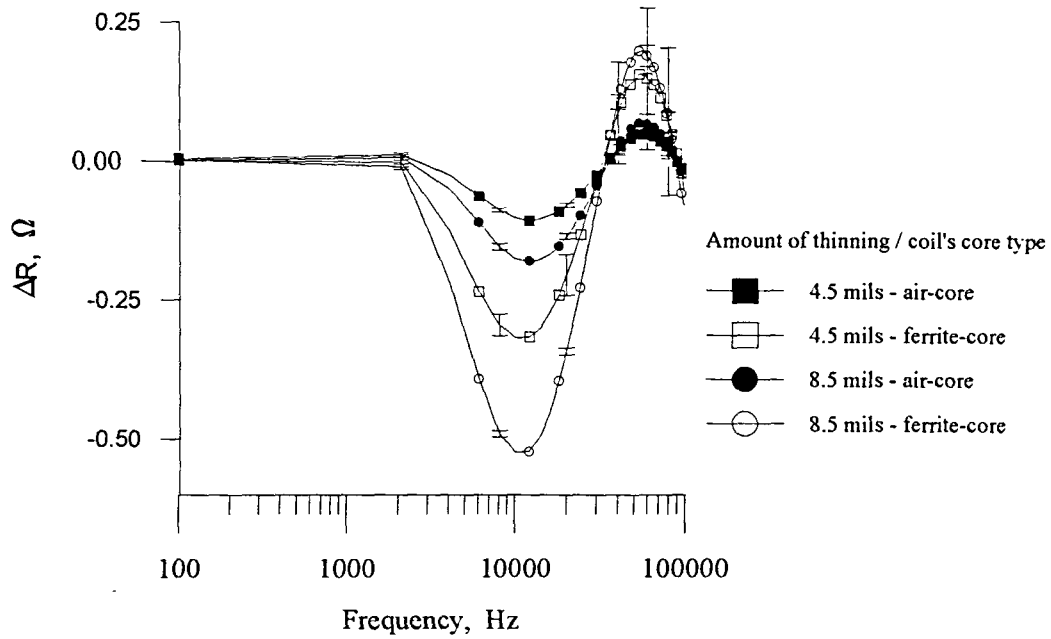


Figure 6.16: Comparison between air and ferrite-core coil signals for second layer thinning

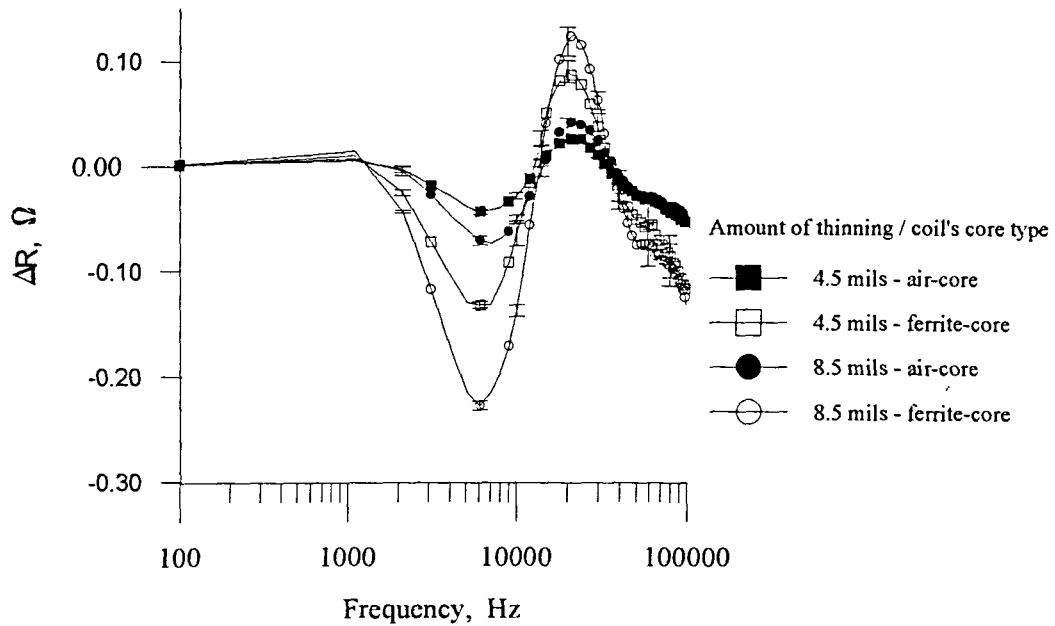


Figure 6.17: Comparison between air and ferrite-core coil signals for bottom surface thinning

example  $\Delta R$ , in relation with that of an identical air-core probe. Comparing several swept frequency measurements for each probe could accurately characterize the ferrite probe's strength factor as a function of frequency. Thus, that ferrite probe could be theoretically modeled with the air-core's parameters, while adjusting the predicted signals by its strength factors.

When direct comparisons are not possible with an identical air-core counterpart, the theoretical model can be used as a tool to determine its parameters in terms of an equivalent air core probe. The procedure would consist of changing one coil parameter at a time, such as the number of turns, in the model until the theory curve matches the experimental swept frequency data for a given known sample set up. This process is simplified if the coil's dimensions are known initially.

These in-depth ferrite probe characterization methods are beyond the scope of this thesis. However, future work in this area is recommended.

## CHAPTER 7. CONCLUSIONS

### 7.1. Summary

This thesis consisted of two main components. First, the quantitative swept-frequency eddy current corrosion characterization technique was examined in both theory and experiment. Precisely wound air-core coils were used in conjunction with an impedance analyzer to accurately measure the coil's resistance change when placed over a 2024 alloy, 2x40 mil skin, aircraft lap splice with and without metal loss due to simulated corrosion. The forward swept frequency solutions compared very well to theory for all four locations of thinning between and below the two layers. The experimental method was first developed by Mitra *et al.* [11] based on earlier work by Moulder *et al.* [9]. The theoretical model was developed by Uzal and Moulder [1], based on previous work by Cheng, Dodd and Deeds [3].

A numerical inversion procedure was used to infer the lap splice's three layer thicknesses, namely the first metal layer, the air gap, and the second metal layer, with two different coils. The results from measurements made on samples with milled flat bottom holes generally showed that the thinned region's location was reliably determined; furthermore, the actual quantities were found to be reasonably accurate for an 8 mm diameter air-core coil, giving an average accuracy of up to 1.8, 1.1 and 2.4 mils for the three thicknesses respectively. These are simply indications of the average  $\pm$  error expected from this type of NDE inversion technique. A larger coil, 14 mm in diameter, yielded even better results. However, it was found that this technique's accuracy decreased when it came to predicting thinning in the

second layer when layer separation was present, with an error of about 7 mils for a 40 mil plate. Yet, the air gap and first layer predictions were still quite reasonable. The accuracy also decreased, although only moderately, when it came to inferring metal loss in artificially corroded samples.

The second objective involved developing eddy current instrument calibration procedures based on the relationship between quantitative resistance changes and the resulting output signal for a given probe-specimen combination. The procedures' results showed that at least two different, and probably most, eddy current instruments can indeed be completely calibrated to measure the impedance change of a probe's test coil. Calibration curves of the output voltage signal vs. the resistance change due to small in-series resistors yielded linear relationships at each measured frequency, the slopes of which were called calibration factors. These calibration factors, in  $V/\Omega$ , were then used to convert flaw signals into resistance changes. These allowed the quantitative corrosion characterization technique to be adapted to commercial instruments. Most of the corrosion tests performed with the impedance analyzer were duplicated with at least two instruments. Their forward results agreed well with theory as well as with the impedance analyzer. The milled samples' inversion results, based on data from eddy current instrument A, were also very accurate; the errors, were on the order of 1.3, 1.6 and 1.6 mils for the three metal-air-metal thicknesses described above. Surprisingly, inversions of the data from the corroded samples taken with the eddy current instrument yielded better accuracy than inversions of those taken with the impedance analyzer, as indicated by the comparisons given in Table 6.8.

As with any NDE technique, there are some limitations that must be identified and understood before implementation. Disagreements and errors in this case can be attributed to various factors. First, very precisely wound coils are required to minimize errors between experiment and the theoretical model. Tilt built into the probe or caused by a misaligned holder, as well as non-uniform thinning due to uneven general corrosion, can each increase the risk of errors as the theoretical model assumes all geometries to be ideal and uniform. The samples used in this thesis allowed the metal loss to be modeled as a uniform air gap between the layers. It is important to realize that corrosion in the form of sparsely distributed deep pits cannot be characterized with this method. One problem that has not been investigated in this thesis is the effect of measuring a corroded area smaller than the probe. Other obvious sources of errors include experimental variability such as inconsistent lift-off, sample warping, or a misaligned probe over a corroded area.

Some important observations about an instrument's characteristic behaviour were discovered during the calibration procedures that apply to most common eddy current instruments. First, the calibration factor was considered to be a measure of the instrument's sensitivity, in  $V/\Omega$ . It was found from circuit analysis and experiment that the two commercial instruments used in this thesis lose sensitivity as the frequency is increased. This is directly related to the probe's impedance, which increases with frequency. Also, higher impedance probes, such as ferrite-core probes, tend to reduce this sensitivity faster with frequency than their air-core counterparts. Thus, an instrument's inherent frequency response must be accounted for when characterizing flaws based on interpretations of multiple

frequency measurements. The calibration factor does this since those inherent responses, unique for any specific probe-instrument combination, are built into the calibration curves.

Overall, these results underscore the feasibility of using existing commercial eddy current instruments to transpose a typical quantitative laboratory technique to the field. In particular, this corrosion detection and characterization method has the potential to be implemented reliably with the instruments already in use by the military and commercial aviation industry. This can translate to a very important time and money saving tool.

## **7.2. Future Work**

The use of ferrite-core probes was briefly studied in this thesis. However, it is recommended that future research be directed toward using these probes for quantitative analyses. Tasks such as using equivalent air core models or finite element models to represent the behaviour of these coils would be useful for improving the practical application of these quantitative NDE methods.

Corrosion occurs in many shapes and sizes. Thus, a study of the effects of measuring corroded areas smaller than the coil itself, including the very common problem associated with the detection of deep pits, would also have practical importance. Lastly, the present corrosion test requires a large range of frequency points that take a long time to experimentally acquire with a typical eddy current instrument, as well as to invert on a workstation computer. A more feasible approach that requires fewer frequencies, such as only about three or four, should be developed. This would save time as well

as reduce the potential for accumulated measurement errors associated with the number of back and forth probe movements required when using a common single frequency commercial instrument in the field.

**BIBLIOGRAPHY**

- [1] Uzal, E. and Moulder, J.C., unpublished work
- [2] Dodd, C.V. and Deeds, W.E. "Analytical Solutions to Eddy-Current Probe-Coil Problems." *Journal of Applied Physics*, Vol. 39, Number 6, May 1968, p 2829-2838.
- [3] Cheng, C.C., Dodd, C.V. and Deeds, W.E. "General Analysis of Probe Coils Near Stratified Conductors." *International Journal of Nondestructive Testing*, Vol. 3, 1971, p 109-129.
- [4] Moulder, J.C. and Uzal, E., unpublished work
- [5] Beissner, R.E. "Boundary Element Model of Eddy Current Flaw Detection in Three Dimensions." *Journal of Applied Physics*, Vol. 60, 1986, p 352-360.
- [6] Nakagawa, N. and Beissner, R.E. "Probability of Tight Crack Detection Via Eddy-Current Inspection." *Review of Progress in Quantitative Nondestructive Evaluation*, Vol. 9, 1990, p 893-899.
- [7] Bowler, J.R., Sabbagh, L.D., Sabbagh, H.A. "A Theoretical and Computational Model of Eddy-Current Probes Incorporating Volume Integral and Conjugate Gradient Methods." *IEEE Transactions on Magnetics*, Vol. 25, No. 3, p 2650-2664, May 1989.
- [8] Udpa, L. and Lord, W. "A Discussion of the Inverse Problem In Electromagnetic NDT." *Review of Progress in Quantitative NDE*, Vol. 5A, 1986, p 375-382.
- [9] Moulder, J.C., Uzal, E. and Rose, J.H. "Thickness and Conductivity of Metallic Layers from Eddy Current Measurements." *Review of Scientific Instruments*, Vol. 63, June 1992, p 3455-3465.
- [10] Uzal, E., Moulder, J.C., Mitra, S., Rose, J.C. "Impedance of Coils Over Layered Metals With Continuously Variable Conductivity and Permeability: Theory and Experiment." *Journal of Applied Physics*, Vol. 74, 1 August 1993, p 2076-2089.

- [11] Mitra, S., Urali, P.S., Uzal, E., Rose, J.H., Moulder, J.C. "Eddy Current Measurements of Corrosion-Related Thinning in Aluminum Lap Splices." *Review of Progress in Quantitative Nondestructive Evaluation*, Vol. 12, 1993, p 2003-2010.
- [12] Hagemaiier, D.J., *Fundamentals of Eddy Current Testing*, American Society for Nondestructive Testing, Columbus, 1990.
- [13] Moulder, J.C. and Gerlitz, J.C., Auld, B.A., Riaziat, M., Jeffries, S. and McFetridge, G. "Calibration Methods for Eddy Current Measurement Systems." *Review of Progress in Quantitative Nondestructive Evaluation*, Vol. 4A, 1985, p 411-420.
- [14] Libby, H.L., *Introduction to Electromagnetic Nondestructive Test Methods*, John Wiley and Sons, Inc., New York, 1971.
- [15] Godard, H.P., Jepson, W.B., Bothwell, M.R., Kane, R.L., *The Corrosion of Light Metals*, John Wiley and Sons, Inc., New York, 1967.
- [16] Davis, J.R. Senior Editor, *Metals Handbook: Corrosion*, Ninth Edition, Volume 13 , ASM International, Metals Park OH, 1987.
- [17] Hatch, J.E., *Aluminum: Properties and Physical Metallurgy*, American Society for Metals, Metals Park OH, 1984.
- [18] Verhoeven, J.D., *Fundamentals of Physical Metallurgy*, John Wiley and Sons, Inc., New York, 1975.
- [19] Fontana, M.G., *Corrosion Engineering*, McGraw-Hill Book Company, New York, 1986.
- [20] ASTM Designation B 177-90, "Standard Test Method of Salt Spray (Fog) Testing", American Society for Testing and Materials, May 1990.
- [21] Patton, T.C., Hsu, D.K., "Investigation of Corrosion in Aluminum/Adhesive Lap-Splices Using Pulse-Echo Ultrasonic Techniques." *Review of Progress in Quantitative Nondestructive Evaluation*, Vol. 12, 1993, p 1995-2002.
- [22] Sadiku, M.N.O, *Elements of Electromagnetics*, Saunders College Publishing, Fort Worth, 1989.
- [23] Natrella, M.G., *Experimental Statistics*, National Bureau of Standards Handbook 91, Department of Commerce, Washington D.C., 1963.

- [24] Bevington, P.R., Robinson, D.K., *Data Reduction and Error Analysis for the Physical Sciences*, Second Edition, McGraw-Hill, Inc., New York, 1992.
- [25] Moulder, J.C., Nakagawa, N., "Characterizing the Performance of Eddy Current Probes Using Photoinductive Field-Mapping." *Research in Nondestructive Evaluation*, 1992, p 221-236.

**APPENDIX A ACCELERATED CORROSION CHAMBER TESTS**

The following corrosion test descriptions and preparations conform to the standard test method found in [20]. The salt spray (fog) test apparatus consists of a fog chamber in which the environmental conditions can be controlled. There is also a salt solution reservoir, a supply of compressed air, and a heater. The samples are placed on supports at an angle of about 10 degrees from the vertical axis, to prevent pooling of the condensed moisture onto the surface. For this particular test, an acidified solution of NaCl is fed into the chamber through atomizing nozzles to create a fog, and maintained at a constant temperature of 95°F. The salt solution is prepared by dissolving 5 parts by weight of NaCl in 95 parts of distilled water. The solution's pH ranges between 6.5 to 7.2 when atomized at 95°F.

**APPENDIX B TABULATED EDDY CURRENT INVERSION RESULTS  
FOR THE MACHINED SAMPLES**

Table B.1. Inferred metal-air-metal layer thicknesses from impedance analyzer swept frequency measurements using coil ISU 2; machined samples thinned in the first layer

<u>Actual thicknesses (mils)</u>			<u>Inferred thicknesses(mils)</u>		
First layer	Air gap	Second layer	First layer	Air gap	Second layer
35.5	4.5	40.0	36.9	5.3	36.9
31.5	8.5	40.0	34.3	9.1	38.9
30.0	10.0	40.0	32.6	10.8	35.4
28.0	12.0	40.0	30.4	12.3	39.8
24.0	16.0	40.0	26.5	15.2	38.8

Table B.2. Inferred metal-air-metal layer thicknesses from impedance analyzer swept frequency measurements using coil ISU 3; machined samples thinned in first, second or both layers

<u>Actual thicknesses (mils)</u>			<u>Inferred thicknesses(mils)</u>		
First layer	Air gap	Second layer	First layer	Air gap	Second layer
35.5	4.5	40.0	36.5	5.0	38.3
31.5	8.5	40.0	32.1	7.9	38.8
28.0	12.0	40.0	28.8	11.9	38.8
40.0	4.5	35.5	42.5	4.5	31.8
40.0	8.5	31.5	41.8	7.7	30.3
40.0	12.0	28.0	40.5	10.4	28.1
35.5	9.0	35.5	36.8	10.3	35.3

Table B.3. Inferred metal-air-metal layer thicknesses from impedance analyzer swept frequency measurements using coil ISU 2 when machined samples' layers have separation but no thinning

<u>Actual thicknesses (mils)</u>			<u>Inferred thicknesses(mils)</u>		
First layer	Air gap	Second layer	First layer	Air gap	Second layer
40.0	4.0	40.0	41.9	4.0	36.3
40.0	12.0	40.0	42.4	11.8	30.3
40.0	16.0	40.0	42.1	16.9	32.6

Table B.4. Inferred metal-air-metal layer thicknesses from impedance analyzer swept frequency measurements using coil ISU 2 when layers have both separation and thinning in first or second layer

<u>Actual thicknesses (mils)</u>			<u>Inferred thicknesses(mils)</u>		
First layer	Air gap	Second layer	First layer	Air gap	Second layer
35.5	8.5	40.0	37.5	9.3	41.3
35.5	12.5	40.0	37.1	13.0	39.9
35.5	16.5	40.0	36.7	17.9	38.7
40.0	8.5	35.5	41.4	9.0	29.6
40.0	12.5	35.5	40.6	11.2	26.4
40.0	16.5	35.5	40.6	13.6	24.2

Table B.5. Inferred metal-air-metal layer thicknesses from instrument A swept frequency measurements using coil ISU 2; machined samples thinned in the first layer

<u>Actual thicknesses (mils)</u>			<u>Inferred thicknesses(mils)</u>		
First layer	Air gap	Second layer	First layer	Air gap	Second layer
35.5	4.5	40.0	33.9	4.7	39.2
31.5	8.5	40.0	33.0	8.5	36.3
30.0	10.0	40.0	32.0	12.4	37.6
28.0	12.0	40.0	30.4	13.4	39.6
24.0	16.0	40.0	27.7	17.5	41.3

Table B.6. Inferred metal-air-metal layer thicknesses from instrument A swept frequency measurements using coil ISU 3; machined samples thinned in first, second or both layers

<u>Actual thicknesses (mils)</u>			<u>Inferred thicknesses(mils)</u>		
First layer	Air gap	Second layer	First layer	Air gap	Second layer
35.5	4.5	40.0	35.2	4.9	40.3
31.5	8.5	40.0	35.1	8.2	39.0
40.0	4.5	35.5	40.5	4.8	34.2
40.0	8.5	31.5	42.0	7.6	31.7
35.5	9.0	35.5	35.3	10.4	37.6

## APPENDIX C GRAPHED EDDY CURRENT INVERSION RESULTS

### C.1. Comparison of Actual Layer Thicknesses to Those Inferred from Impedance Analyzer and Instrument A Swept Frequency Measurements

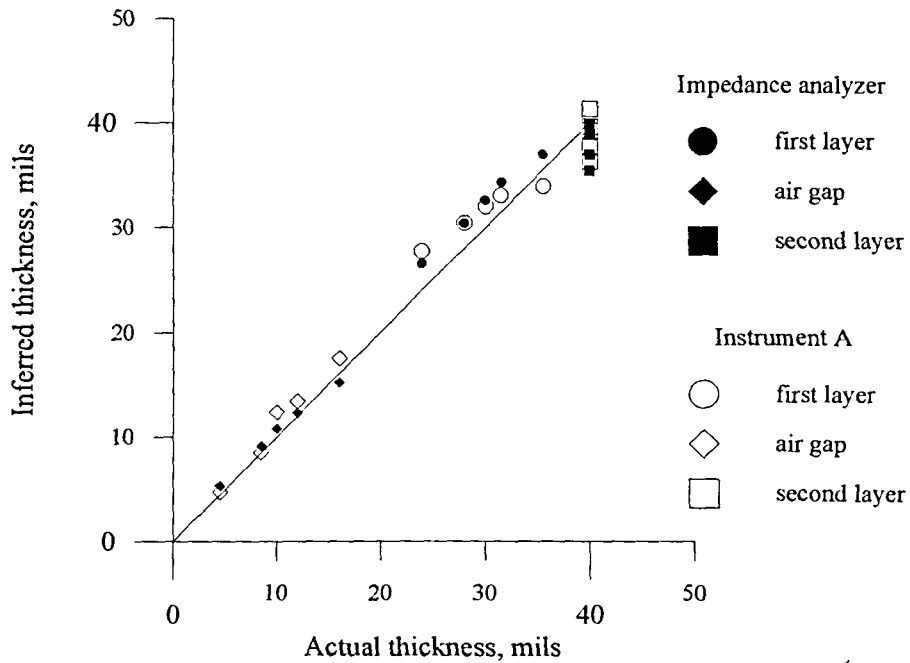


Figure C.1: Machined samples thinned in the first layer using coil ISU 2

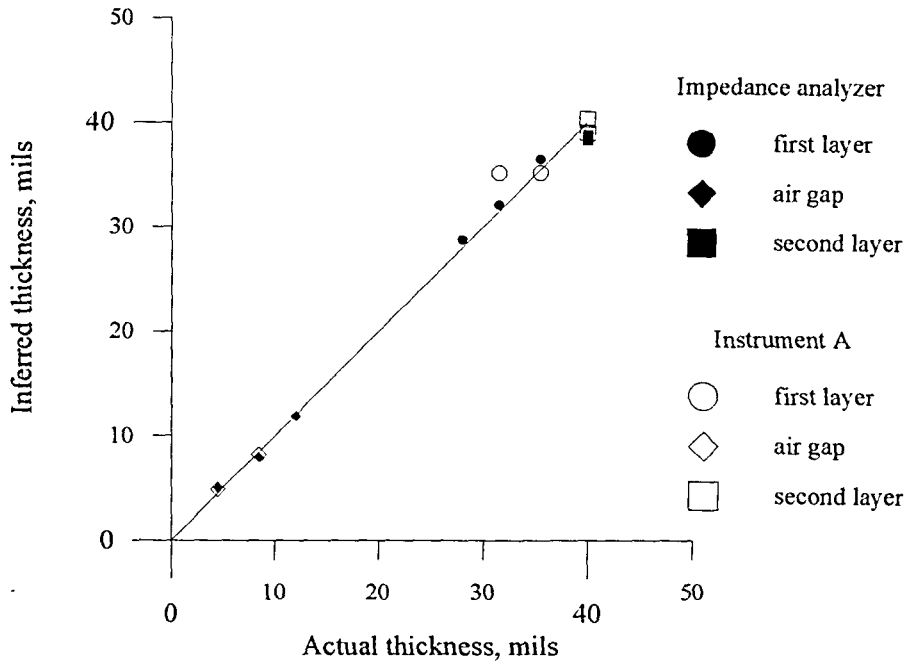


Figure C.2: Machined samples thinned in the first layer using coil ISU 3

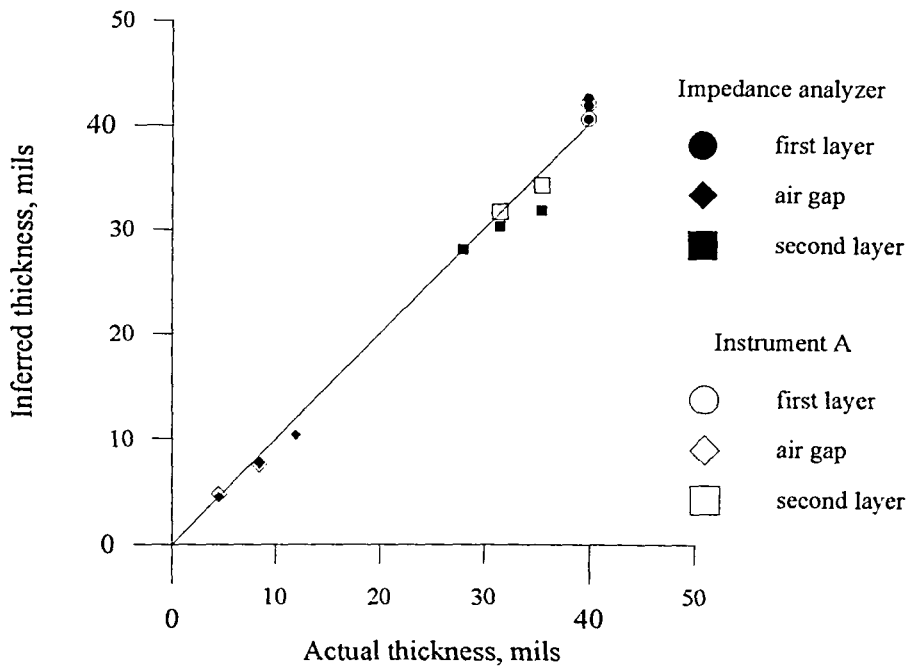


Figure C.3: Machined samples thinned in the second layer using coil ISU 3

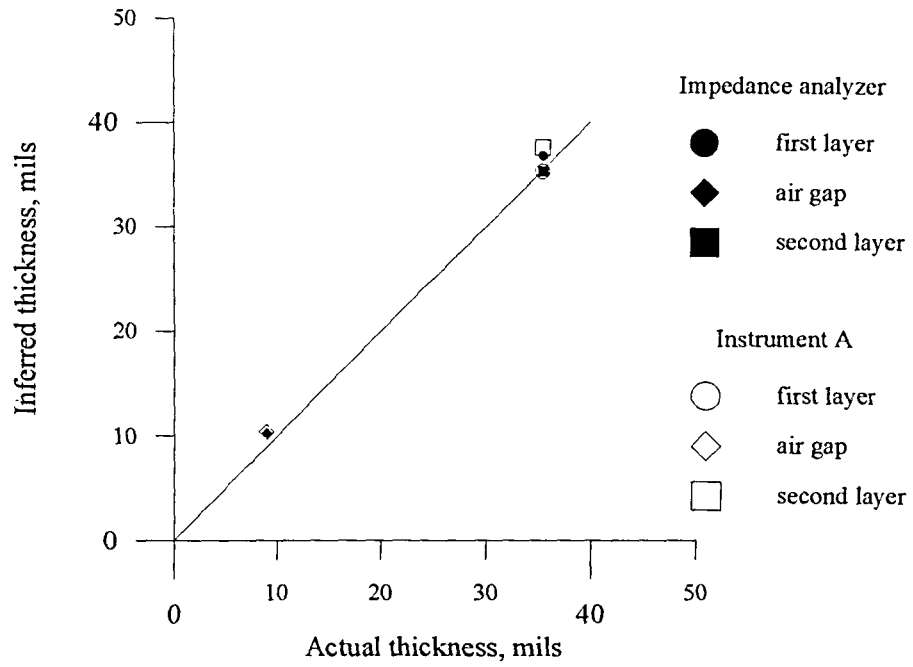


Figure C.4: Machined samples thinned in both layers using coil ISU 3

### C.2. Inferred Layer Thicknesses in the Presence of Plate Separation

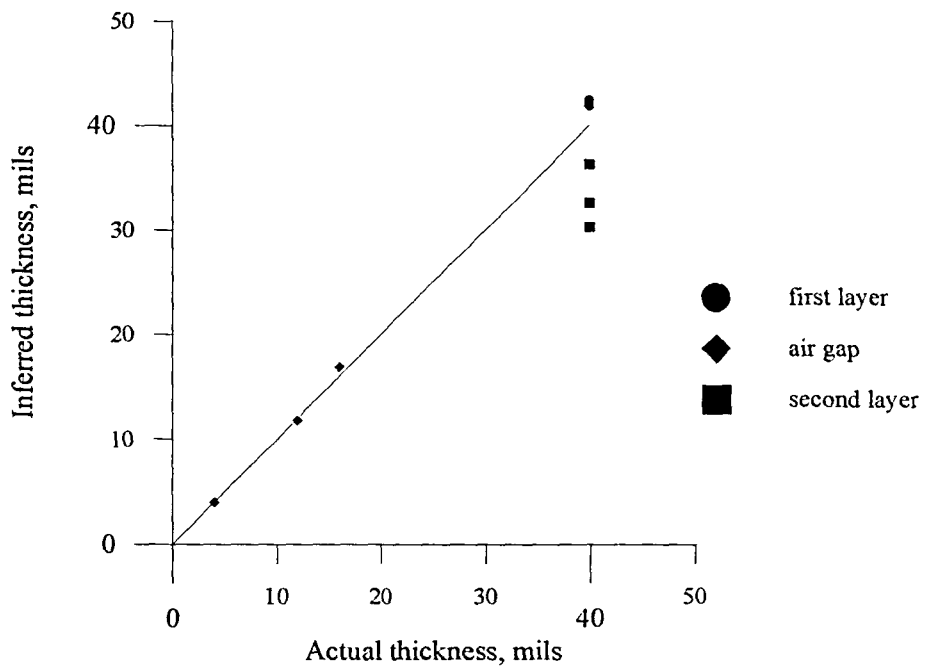


Figure C.5: Machined samples' layers with separation, but no thinning, using coil ISU 2 and impedance analyzer

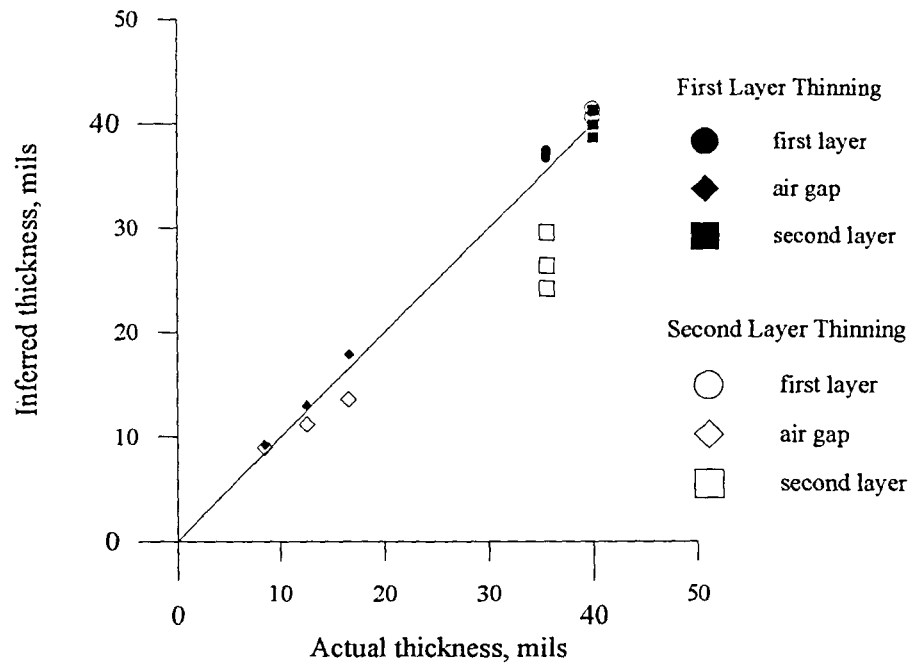


Figure C.6: Machined samples layers with both separation and thinning in first or second layer, using coil ISU 2 and impedance analyzer